Apropos 17

Advanced Properties and Processes in Optoelectronic Materials and Systems
30 September – 1 October, 2020

Sattelite Event

Lithuania-Poland Workshop
on Physics and Technology

CONFERENCE PROGRAMME

Center for Physical Sciences and Technology (FTMC), Vilnius, Lithuania
Venue: FTMC at Sunrise Valley, Saulėtekio Ave. 3, Vilnius, Lithuania

30 September		
8:00-9:00		REGISTRATION
9:00-9:15		**CONFERENCE OPENING CEREMONY** **Gintaras Valušis** Director of Center for Physical Sciences and Technology Chair of Apropos 17 conference
9:15-10:35		**Section 1: Semiconductor nanostructures and advanced photonics systems** **Chair Prof. *Carlito Jr.Salonga Ponseca***
9:15-9:45	**Inv 1**	**Linas Minkevičius** *(Center for Physical Sciences and Technology, Vilnius, Lithuania)* Review of innovative diffractive elements for Terahertz imaging applications
9:45-10:15	**Inv2**	**Ramūnas Aleksiejūnas** *(Vilnius University, Lithuania)* Impact of alloy disorder induced localization on hole diffusion in highly excited c-plane and m-plane InGaN quantum wells
10:15-10:35	O1	Janusz Sadowski (*University of Warsaw, Institute of Physics, Warsaw, Poland, Linnaeus University, Sweden)* MoTe2 transition metal dichalcogenide grown by molecular beam epitaxy – polytypes, structural and electrical properties
10:35-11:00		**Coffee break**
11:00-13:00		**Section 2: Nano and Biophotonics** **Chair Dr. *Kaibo Zheng***
11:00-11:30	**Inv3**	**Šarūnas Meškinis** *(Kaunas University of Technology, Lithuania)* Direct synthesis of the graphene on Si(100) substrate for solar cell applications

11:30-12:00	**Inv4**	**Dovydas Banevičius** *(Vilnius University, Lithuania)* Naphthyridine-based deep-blue TADF OLEDs with low efficiency roll-off
12:00-12:20	O2	Rusnė Ivaškevičiūtė-Povilauskienė *(Center for Physical Sciences and Technology, Vilnius, Lithuania)* All-optical modulation of graphene layers
12:20-12:40	O3	Lena Golubewa *(Center for Physical Sciences and Technology, Vilnius, Lithuania)* Raman spectroscopic investigation of multi-walled carbon nanotubes mediated neutrophil activation
12:40-13:00	O4	Adil Rehman (*Institute of High Pressure Physics, Warsaw, Poland*) Modulation of electrical and noise characteristics of carbon nanotubes based devices
13:00-14:00		**Lunch**
14:00-15:50		***Special session:*** **Ultrafast THz techniques** **Chair Dr.** ***Ignas Grigelionis***
14:00-14:30	**Inv5**	**Carlito S. Ponseca, Jr.** (*Linköping University, Sweden*) - Ultrafast transient spectroscopy of organic and hybrid solar cells
14:30-14:50	O5	Kaibo Zheng *(Lund University, Sweden, Technical University of Denmark, Danmark)* Ultrafast spectroscopy of Quantum dot solar cells
14:50-15:10	O6	Ričardas Norkus *(Center for Physical Sciences and Technology, Vilnius, Lithuania)* Terahertz emission from a bulk GaSe crystal excited by above-bandgap photons
15:10-15:30	O7	Daniil Pashnev *(Center for Physical Sciences and Technology, Vilnius, Lithuania)* Investigation of two-dimensional plasma resonances in grating-gated AlGaN/GaN heterostructures by terahertz time domain spectroscopy
15:30-15:50	O8	Marek Maciaszek (*University of Warsaw, Poland)* On the origin of the 4.1 eV luminescence in hexagonal boron nitride
15:50-16:15		**Coffee break**
16:15-18:20		**Section 1: Semiconductor nanostructures and advanced photonics systems** **Chair Prof.** ***Šarūnas Meškinis***
16:15-16:45	**Inv6**	**Tadas Malinauskas** *(Vilnius University, Lithuania)* Remote epitaxy of GaN via Graphene
16:45-17:05	O9	Ivan Yahniuk (*Institute of High Pressure Physics, Warsaw, Poland*) Temperature-& Pressure-induced transitions in HgTe QWs
17:05-17:20	O10	Roman M. Balagula *(Center for Physical Sciences and Technology, Vilnius, Lithuania)* Annealing-induced reduction of strain in GaAs/GaNAs core-shell nanowires
17:20-17:40	O11	Andrea Zelioli *(University of Modena, Italia)* GaInAs/GaAs Quantum Structures For Near Infrared Vertical-External-Cavity Surface-Emitting Lasers
17:40-18:00	O12	Simona Pūkienė *(Center for Physical Sciences and Technology, Vilnius, Lithuania)* A3-B5 QW structures for IR range optoelectronic devices
18:00-19:30		**Poster session (18 posters)** **Coffee and Snaps**

1 October		
9:00-11:00		***Satellite Event:*** **Lithuanian Polish Workshop** **Chair Prof. *Janusz Sadowski***
9:00-9:10		**WORKSHOP OPENING CEREMONY** Ambassador Urszula Doroszewska, Embassy of Poland Jerzy Łusakowski (Chair from Poland)
9:10-9:35	**Inv7**	**Nerija Žurauskienė** *(Center for Physical Sciences and Technology, Vilnius, Lithuania)* Magnetoresistance Relaxation Phenomena in Nanostructured Lanthanum Manganite Films
9:35-10:00	**Inv8**	**Wojciech Pacuski** (*University of Warsaw, Poland)* Narrow excitonic lines and large-scale homogeneity of transition metal dichalcogenides grown by MBE on hBN
10:00-10:20	O13	Maksym Dub (*Institute of High Pressure Physics, Warsaw, Poland*) Graphene gate GaN/AlGaN field effects transistors for THz detection
10:20-10:40	O14	Maria Szoła (*Institute of High Pressure Physics, Warsaw, Poland*) THz magnetospectroscopy of HgCdTe bulk crystals with different Cd content
10:40-11:00	O15	Paweł Komorowski (*Warsaw University of Technology, Poland*) Machine learning enhanced design of diffractive optical elements
11:00-11:25		**Coffee break**
11:25-13:05		**Section 3: Ultrafast and THz phenomena** **Chair Dr. *Linas Minkevičius***
11:25-11:55	**Inv9**	**Alvydas Lisauskas** (*Vilnius University and Institute of High Pressure Physics, Warsaw, Poland)* THz detectors and sources fabricated with CMOS technologies
11:55-12:25	**Inv10**	**Guillaume Ducournau** *(Université Lille, France)* THz communications and advanced RF characterization enabled by THz photonics
12:25-12:45	O16	Dmytro B. But (*Institute of High Pressure Physics, Warsaw, Poland*) Antenna Characterization of Monolithically Integrated Detectors for 0.62 THz
12:45-13:05	O17	Domas Jokubauskis *(Center for Physical Sciences and Technology, Vilnius, Lithuania)* Phase contrast sub THz imaging and applications
13:05-14:00		**Lunch**
14:00-15:50		**Section 3: Ultrafast and THz phenomena** **Chair Prof. *Alvydas Lisauskas***
14:00-14:30	Inv11	**Vincas Tamošiūnas** *(Center for Physical Sciences and Technology, Vilnius, Vilnius University, Lithuania)* Reflectance spectra of selective emitter solar cells in terahertz and sub-terahertz ranges
14:30-14:50	O18	Dmitri V. Lioubtchenko (*KTH Royal Institute of Technology, Stockholm, Sweden)* Effect of lengths, diameters, and density of silver nanowire layers on terahertz conductivity

14:50-15:10	O19	Ieva Žičkienė *(Center for Physical Sciences and Technology, Vilnius, Lithuania)* Terahertz radiation induced by surface ballistic photogalvanic effect in GaAs LIPSS structures
15:10-15:30	O20	Pavlo Sai (*Institute of High Pressure Physics, Warsaw, Warsaw University of Technology, Poland*) AlGaN/GaN dual grating gate structures investigated in high magnetic field
15:30-15:50	O21	Vladislovas Čižas *(Center for Physical Sciences and Technology, Vilnius, Lithuania)* Fractional frequencies in microwave response of GaAs/AlGaAs superlattices
15:50-16:15		**Coffee break**
16:15-17:35		**Section 4: Organics for Optoelectronics** **Chair Dr. Prof. *Nerija Žurauskienė***
16:15-16:35	O22	**Yuri Svirko** *(University of Eastern Finland, Joensuu, Finland)* Light-induced currents and THz emission from graphene
16:35-16:55	O23	Ernesta Poceviciute *(Center for Physical Sciences and Technology, Vilnius, Lithuania)* Studies of Receptor and Its Ligand Interaction Using FRET and TIRF Microscopy
16:55-17:15	O24	Edvinas Navakauskas *(Center for Physical Sciences and Technology, Vilnius, Lithuania)* Structure determination of HEWL protein aggregates at liquid interfaces
17:15-17:35	O25	Wanessa Melo *(Center for Physical Sciences and Technology, Vilnius, Lithuania)* Antimicrobial photodynamic therapy: an alternative to overcome the biofilm resistance
17:40		**Closing Remarks**

List of posters

P1-1 Algirdas Jasinskas Optically pumped semiconductor lasers based on InGaAs/GaAs and GaAsBi/GaAs quantum wells

P1-2 Jonas Gradauskas Three components of photovoltage simultaneously induced across GaAs p-n junction

P1-3 Karolis Stašys Bismide-based Intersubband devices for Mid-Infrared Applications

P1-4 Linas Ardaravičius Determination of electron drift velocity from hot-electron effect in ZnO epilayers and AlGaN/GaN heterostructures

P1-5 Roman Balagula Optical properties of GeSi/Si quantum dots in mid- and far-IR range

P2-1 Agnė Zdaniauskienė In-situ SHINERS analysis of SAM from thiols with imidazole ring and intrachain amide groups

P2-2 Karolina Maleckaitė Polarity sensors based on thiophene-substituted BODIPY molecular rotors

P2-3 Rokas Gegevičius Energy Barriers in MAPbI3 Perovskite Films

P2-4 Rokas Jasiunas Benefits of MAPbI3 perovskite doping by Sr2+

P2-5 Rugilė Lukaševičiūtė Activity measurements of GMC superfamily flavoenzymes using Amplex Red assay

P2-6 Šarūnas Jankauskas Structural defect behavior of thermally annealed graphene, directly synthesized on Si(100) substrate using MW-PECVD

P2-7 Vaidas Pudžaitis In-situ probing of SAM and tBLM layer formation on nanostructured gold by ATR-SEIRAS

P3-1 Andrius Kamarauskas Impact of thin low specific conductivity layer on Fano resonance amplitude in an array of split ring resonators

P3-2 Ieva Matulaitienė Black silicon based substrates for surface enhanced Raman spectroscopy

P3-3 Ivan Yahniuk Terahertz detection and noise properties of (Cd1-xZnx)3As2

P3-4 Juozas Vyšniauskas Enhanced sensitivity AlGaN/GaN HEMT terahertz detector without ungated regions

P3-5 Liang Qi Performance of Titanium-based Microbolometers for Monitoring of Spatial Beam Profile in Terahertz Time-Domain Systems

P3-6 Paulius Mackonis Laser system for pumping THz and coherent X-ray sources of secondary radiation

Optically pumped semiconductor lasers based on InGaAs/GaAs and GaAsBi/GaAs quantum wells

Algirdas Jasinskas, Simona Pūkienė, Lukas Jočionis, Bronislovas Čechavičius, Ada Gajauskaitė and Renata Butkutė

Center for Physical Sciences and Technology, Saulėtekio av. 3, LT-10257 Vilnius, Lithuania

Apropos 17

2020 September 30 – October 1, Vilnius, Lithuania

algirdas.jasinskas@ftmc.lt

Motivation

Low cost, reliable and compact electrically injected laser diodes have become irreplaceable in fields such as laser pumping, communications, medicine and more [1]. However, for some applications it is more convenient to have laser irradiation come out vertically from the device, rather than from its edge as in the case of laser diodes. More complex vertical cavity lasers exhibit this feature. Additionally, as in the case of vertical external cavity surface emitting lasers (VECSELS) – optical pumping allows achieving much greater output powers and beam quality while still maintaining wavelength versatility [2]. Essentially, these lasers combine advantages of both semiconductor and solid-state lasers, therefore they are very attractive and in great demand.

The goal of this work was to produce and characterize NIR region (1-1.2 µm) optically pumped lasers based on two different gain materials – GaAsBi and InGaAs. The working principle of a VECSEL is shown in Fig. 1. Semiconductor chip with quantum well gain section is mounted on a heatsink and pumped by a diode laser. The resonator cavity is formed by using an external mirror.

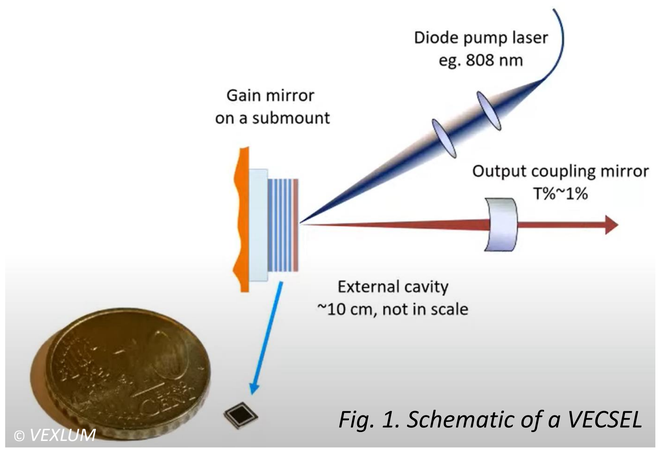

Fig. 1. Schematic of a VECSEL

Sample preparation and characterization

Resonant Periodic Gain (RPG) design (Fig. 2) was used in which a standing electromagnetic wave is formed at lasing wavelength which stimulates quantum well emission. QWs were placed in groups of 2-4 to reduce the overall thickness of the structure and improve thermal properties. Molecular Beam Epitaxy (MBE) equipment was used for growth of the samples. 28.5 period GaAs/AlAs DBR was grown on GaAs substrate, followed by the gain region (QWs and spacers), window layer and capping layer. Photoluminescence (PL), Reflectance and Atomic Force Microscopy (AFM) measurements were performed to characterize the grown lasers.

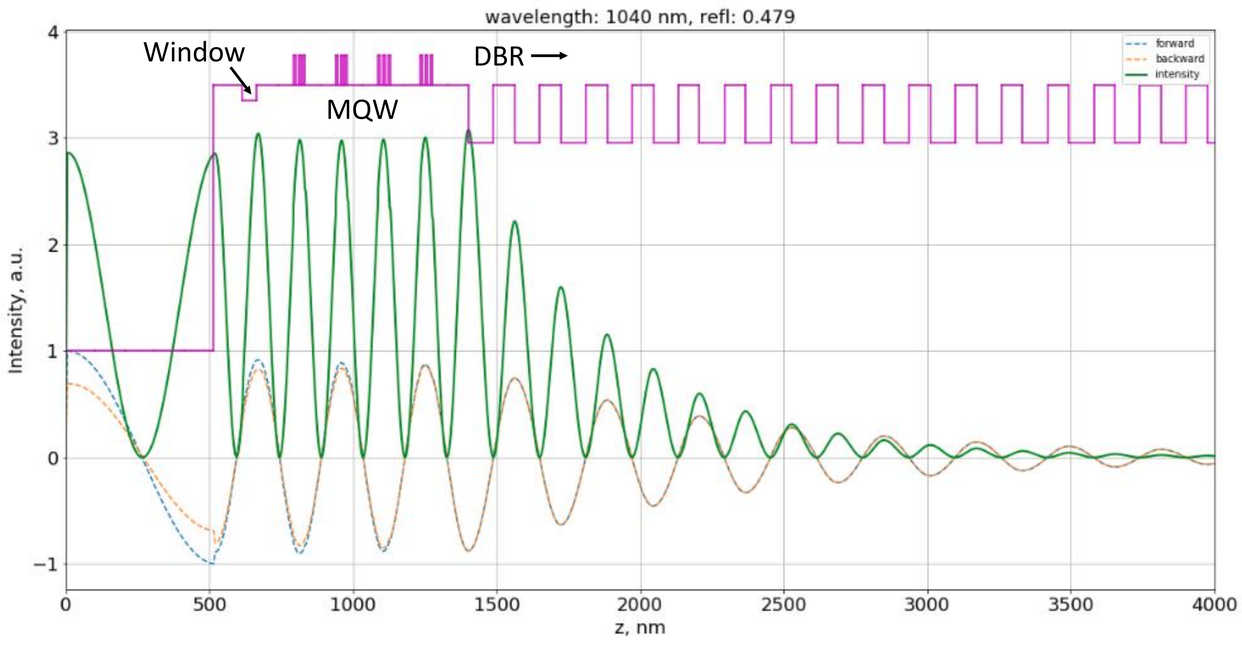

Fig. 2. RPG design of one of the grown VECSEL structures. Purple line represents refractive index profile and green curve – electromagnetic field intensity.

GaAsBi VECSELs

Lasers based on GaAsBi QWs have shown PL in longer wavelengths than InGaAs QWs, however, due to technological challenges associated with GaAsBi MBE growth, it was often difficult to control Bi incorporation precisely and match the QW emission peak with resonant cavity wavelength (sample VGA0385).

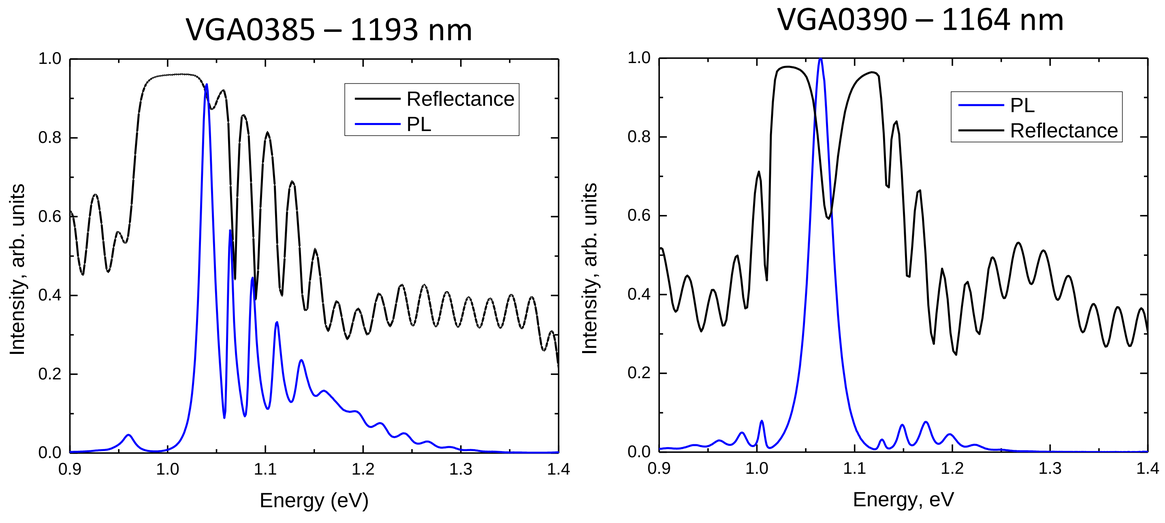

Fig. 3. Reflectance (black curve) and room temperature PL (blue curve) measurements of GaAsBi MQW VECSELS. The central wavelengths of these lasers are 1193 and 1164 nm.

After many growth runs, sample VGA0390 exhibited PL peak at around 1164 nm well matched with the reflectivity dip of cavity resonance.

InGaAs VECSELs

Very similar laser structures were grown by changing QW material from GaAsBi to InGaAs. While using this compound, PL intensity increased by around 3 orders of magnitude and the results were much more reproducible than in the case of bismides.

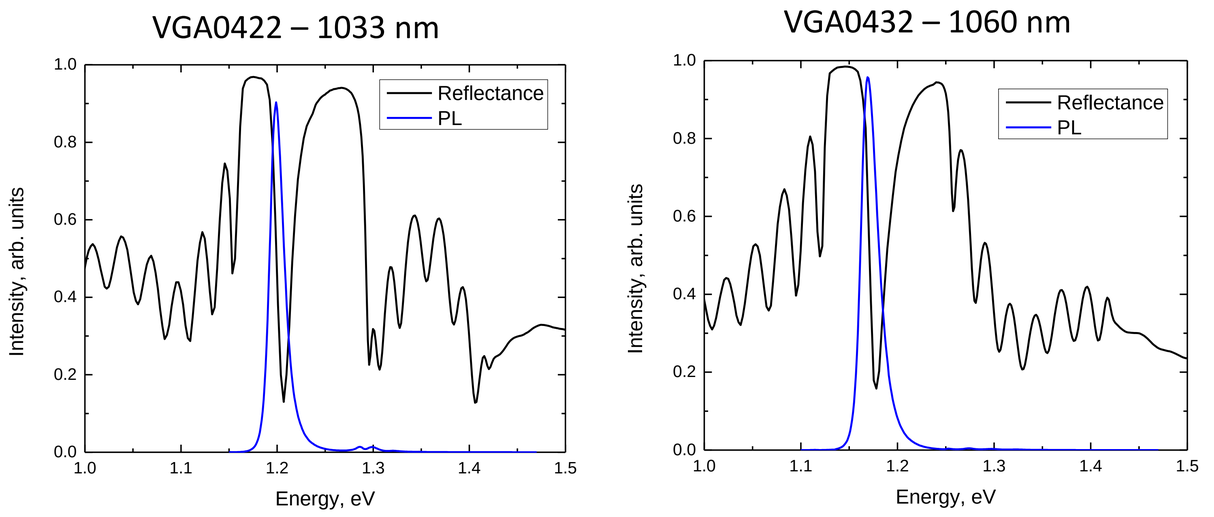

Fig. 3. Reflectance (black curve) and room temperature PL (blue curve) measurements of InGaAs MQW VECSELS. The central wavelengths of these lasers are 1033 and 1060 nm.

Surface quality

AFM measurements have shown dislocations going across all the surface of InGaAs QW samples (VGA0456) due to strain relaxation. While this roughness is very low and gets smoothened as the next VECSEL layers are deposited (VGA0432) this definitely shows, that strain relaxation would be a major issue when trying to reach longer wavelengths with this material.

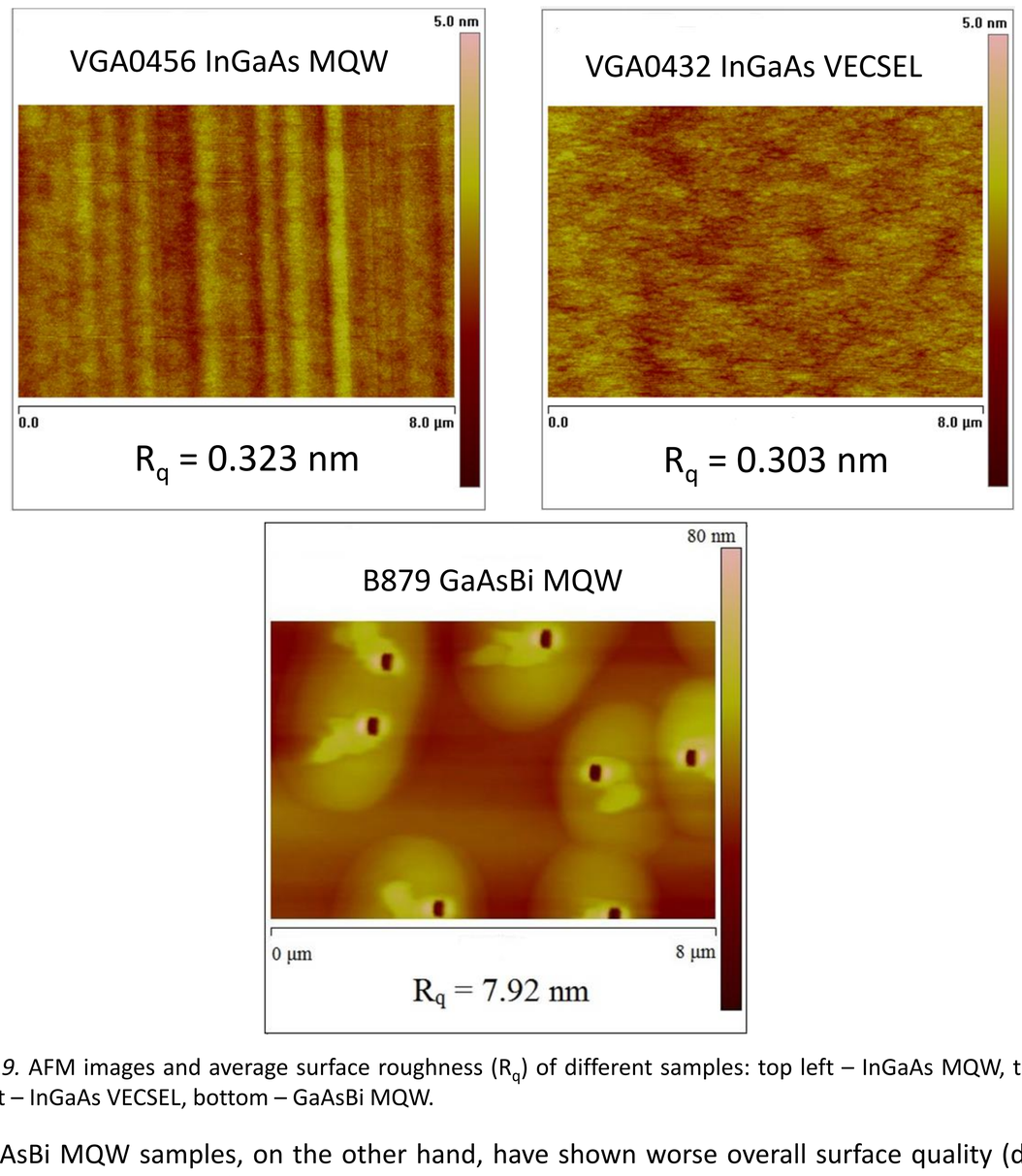

Fig. 9. AFM images and average surface roughness (R_q) of different samples: top left – InGaAs MQW, top right – InGaAs VECSEL, bottom – GaAsBi MQW.

GaAsBi MQW samples, on the other hand, have shown worse overall surface quality (due to extreme growth conditions) which also gets improved as the top VECSEL layers are grown. As expected, no signs of similar dislocations were observed due to more rapid bandgap reduction of bismides.

Conclusions

The grown VECSEL structures are yet to be measured in an optical pumping setup, but the primary characterization revealed high potential of these samples. Reflectivity dip at the center of Bragg mirror indicated standing electromagnetic wave which matched with desired lasing wavelength well and the emission wavelength of the QWs was matched with the resonant wavelength.

Structures based on InGaAs/GaAs quantum wells exhibited much higher intensities and were found to be much more reliable, however, bismide based structures have the potential to reach longer wavelengths while still using GaAs technological platform.

References

[1] D. Patil; Semiconductor laser diode: technology and applications, Intech (2012) pp. 217-219.
[2] M. Guina et al., Journal of Physics D: Applied Physics 50 (2017).

Three components of photovoltage simultaneously induced across GaAs p-n junction

Jonas Gradauskas[1,2], Steponas Ašmontas[1], Algirdas Sužiedėlis[1], Aldis Šilėnas[1], Aurimas Čerškus[1,2], Viktoras Vaičikauskas[1], Edmundas Širmulis[1], Ovidijus Žalys[1], Oleksandr Masalskyi[2]

jonas@pfi.lt

[1]*Center for Physical Sciences and Technology, Vilnius, Lithuania*

[2]*Vilnius Gediminas Technical University, Vilnius, Lithuania*

INTRODUCTION

According to the Shockley-Queisser theory, only photons having energy hv close to a semiconductor forbidden energy gap E_g are used effectively for electrical power generation. Lower energy photons are assumed as not absorbed at all, while the residual extra energy of higher energy photons is reckoned in only through the process of carrier thermalization.

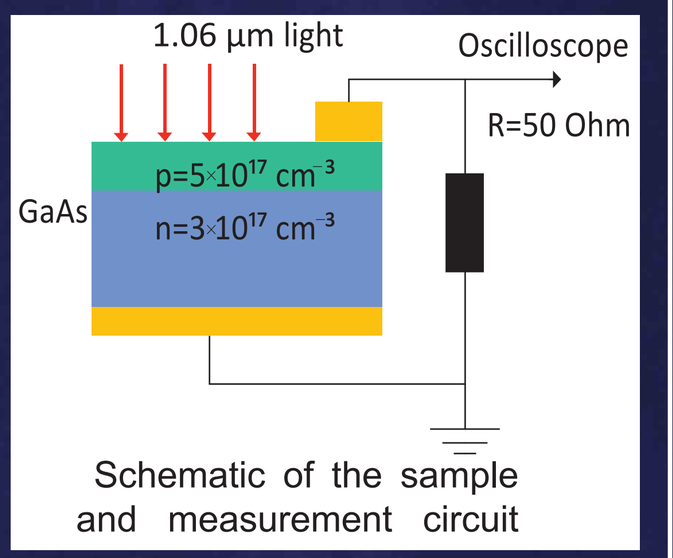

Schematic of the sample and measurement circuit

There again, hot carriers can be generated by the infrared radiation (“not absorbed at all”) as well as by the photons supplying the mentioned extra residual energy. And the intraband light absorption has been demonstrated to rise a hot carrier photoemf across a semiconductor p-n junction illuminated with a CO_2 laser (hν=1.17 meV) radiation [1,2]. The photoemf had polarity opposite to that of the classical carrier generation-induced emf.

We present experimental evidence of direct hot carrier influence on the net photovoltage formation across a semiconductor p-n junction. As an object of investigation, GaAs (E_g=1.42 eV) p-n junction was illuminated with 25 ns-long laser pulses of 1.06 μm wavelength (hν=1.17 eV).Such experimental assortment allowed to investigate simultaneous rise of the hot carrier photovoltage andthe classical photovoltage resulting from carrier generation due to two-photon absorption [3,4].

RESULTS. THREE PHOTOVOLTAGE PULSES

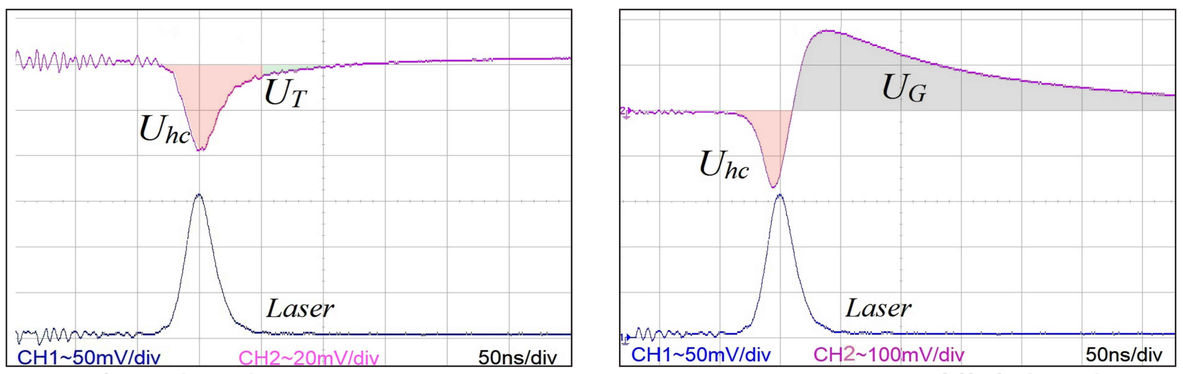

Low level — High level

Experimental traces of photovoltage across GaAs p-n junction at different excitation levels. No bias voltage is applied.

Simultaneous rise of hot carrier U_{hc} (reddish area) and carrier generation-induced U_G (bluish area) photovoltages is obvious. Thermalization-caused component U_T (green area) can be seen following the U_{hc} in the case of low excitation level

RESULTS. PHOTORESTONSE

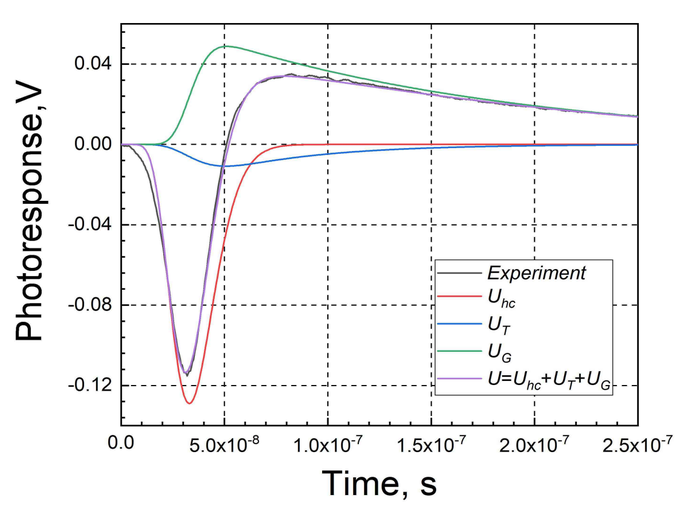

Photoresponse across GaAs p-n junction at moderate excitation level

Experimental photoresponse (black); its components due to hot carriers (red), thermalisation (blue), generation (green), and their sum (violet)

RESULTS. BOTH PHOTOVOLTAGES vs INTENSITY

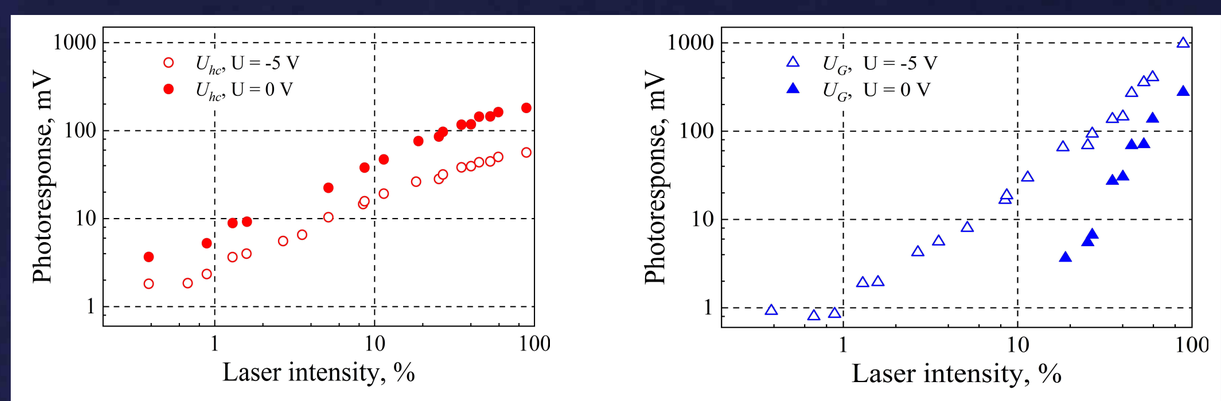

Hot Carrier PV — Generation PV

Dependence of hot carrier photovoltage U_{hc} (red dots) and generation-induced photovoltage U_G (blue dots) across GaAs p-n junction on laser intensity at zero bias (solid dots) and -5 V of reverse bias voltage (open dots)

The reverse bias voltage acts against the hot carrier photovoltage formation.

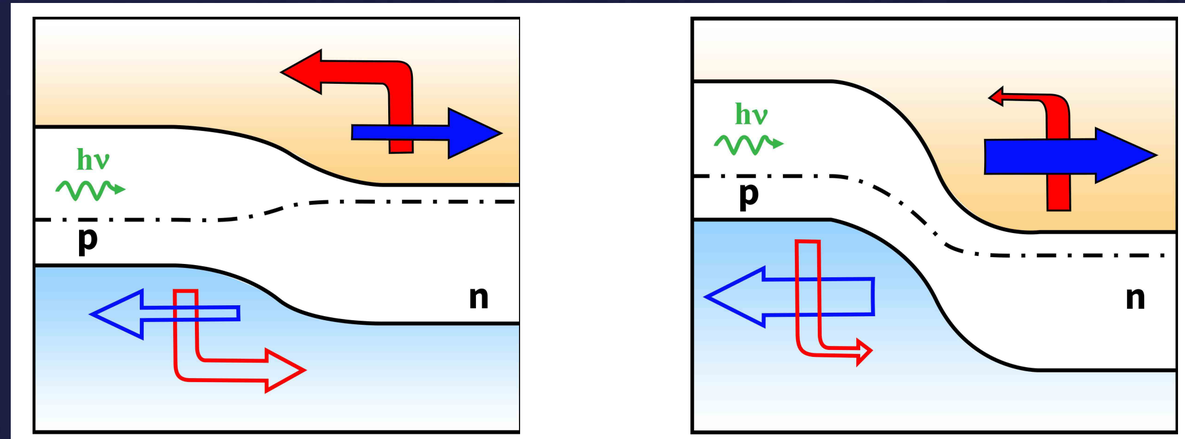

Forward bias — Reverse bias

Schematic description of hot carrier (red arrows) and generation-induced (blue arrows) photocurrents as forward and reverse bias voltage is applied. Hollow arrows stand for flows of holes

CONCLUSIONS

- In general, photoresponse in a p-n junction consists of three simultaneous components induced by:
  - ✔ electron-hole pair generation,
  - ✔ hot carriers,
  - ✔ lattice heating after thermalisation.
- Hot carrier photovoltage across a p-n junction
  - ✔ is evidenced experimentally,
  - ✔ rises prior to the thermalization,
  - ✔ opposes the classical generation-induced photovoltage.
- Forward bias voltage increases the input of the hot carrier photovoltage.

(*How does the classical photovoltage bias a p-n junction*?)

- Hot carrier photovoltage may be the reason of still unattainable Schockley-Queisser limit.

ACKNOWLEDGMENT

This work was in part supported by the Research Council of Lithuania (grant No. 01.2.2-LMT-K-718-01-0050).

REFERENCES

1.S. Ašmontas, J. Gradauskas, D. Seliuta, E. Širmulis. Photoelectric properties of nonuniform semiconductor under infrared laser radiation. Proc. SPIE4423, 18–27 (2001).
2.F. Encinas-Sanz, J.M. Guerra. Laser-induced hot carrier photovoltaic effects in semiconductor junctions. Progress in Quantum Electronics 27, 267 (2003).
3.S. Ašmontas, J. Gradauskas, A. Sužiedėlis, A. Šilėnas, E. Širmulis, V. Švedas, V. Vaičikauskas, and O. Žalys, Appl. Phys. Lett. 113, 071103 (2018).
4.J. Gradauskas, S. Ašmontas, A. Sužiedėlis, A. Šilėnas, V. Vaičikauskas, A. Čerškus, O. Žalys, O. Masalskyi.Unfolding hot carrier impact in photovoltage across a p-n junction. Journal of Appl. Phys. (in press)

Bismide-based Intersubband devices for Mid-Infrared Applications

Karolis Stašys[1], Ričardas Norkus[1], Sandra Stanionytė[1] and Jan Devenson[1]
[1]*Center for Physical Sciences and Technology, Sauletekio av. 3, LT-10257, Vilnius, Lithuania.*
Email: karolis.stasys@ftmc.lt

FIZINIŲ IR TECHNOLOGIJOS MOKSLŲ CENTRAS

Abstract:
Intersubband devices such as Quantum cascade lasers (QCLs) are considered now as standard light sources for many chemical sensing applications in the mid-infrared above 4 µm. Performances of diode lasers rapidly degrade below 3 µm due to fundamental limitations such as increasing influence of nonradiative Auger recombination. But this obstacle can be resolved by using bismides materials such as InAsBi/Al(As)Sb and InGaAsBi/AlAsSb in QCL superlattices structure [1,2]. In this work the MBE growth technique for the epitaxy of InAsBi/Al(As)Sb and InGaAs/AlAsSb quantum wells has been developed. Bismuth containing superlattices exhibited excellent interface contrast and crystalline quality. Obtained growth conditions can be considered as suitable for the growth of Bismide-based intersubband devices.

Main goal and challenges:
The main goal is the development of molecular beam epitaxy (MBE) procedure for the growth of InAsBi/Al(As)Sb and InGaAsBi/AlAsSb superlattices, which will be suitable for integration as active quantum wells into InAs/Al(As)Sb and InGaAs/AlAsSb injectors in Quantum Cascade Laser structures. There are two steps for each material system associated with the growth of such structures: 1) epitaxy of low temperature grown bismuth containing superlattices and 2) integration of low temperature grown bismide superlattices into high temperature grown superlattices – 4 stages in overall.
The challenge is that the main difference between these two material systems is that despite compositional similarity these two material systems are dedicated for the growth on different substrates – InAsBi/Al(As)Sb on InAs substrates, while InGaAsBi/AlAsSb on InP substrates. InAs/Al(As)Sb can be considered as lattice matched system while InGaAsBi/AlAsSb is strain balanced and more complicated for the growth. Advantage of the InAs-based system is that it has larger conduction band offset, thus, better carrier confinement, slightly lower electron effective mass, and also entire laser structure can be grown in the same process as no overgrowth is needed. InP based system mainly takes an advantage of better InP thermal conductivity. [3]

MBE growth of InGaAsBi/AlAsSb on (100) InP substrates:
As a first step, in order to find appropriate growth conditions for $In_{0.7}Ga_{0.3}As_{1-x}Bi_x$ layers a set of samples have been grown on InP substrates at different growth temperatures varying As/Ga and As/Bi flux ratios. All samples were grown using solid source Veeco GEN Xplor molecular beam epitaxy (MBE) system, equipped with SUMMO group III element sources, Veeco As and Sb valved cracker sources and conventional Dual Filament bismuth source. The substrate temperature was controlled by a thermocouple (TC) and kSA BandIT broadband pyrometry module. The kSA 400 Reflection High-Energy Electron Diffraction (RHEED) system was used for in-situ surface characterisation. Each substrate prior to be loaded into the growth chamber has been outgassed at 200 ℃ in the load lock and later at 300 ℃ in the buffer chamber. The thicknesses of InGaAs buffer layers in samples varied from 100 nm to 270 nm depending on observation of RHEED pattern quality to decide if buffer layers is sufficiently smooth. All the samples were grown at the ~0.5 monolayer/s growth rate. InGaAsBi layers were grown at temperatures, which are commonly used for the growth of ternary bismide alloys: 280 ˚C, 300 ˚C, and 320 ˚C. To ensure that only temperature will have an influence, the Bi/InGa ratio was kept the same. All grown samples had smooth surface and exhibited decent incorporation of bismuth. X-Ray measurement results are shown in Figure 1.
Samples grown at lower temperature have higher amount of incorporated bismuth. However, samples grown at temperatures 280 ˚C (5.3% Bi) and 300 ˚C (5.1% Bi) have difference of only 0.2% while the amount of incorporated bismuth in sample grown at 280 ˚C dropped to 4.2%. Moreover, it seems that the layer grown at 300 ˚C has better crystalline quality, as it has sharper main peak and visible fringes around bismide corresponding peak. Therefore, the temperature of 300 ˚C was stated to be the optimal temperature for the growth of InGaAsBi layers.

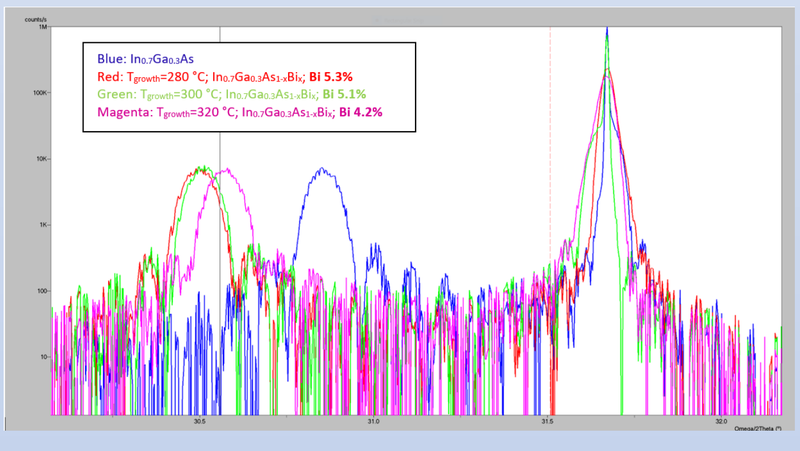

Fig. 1. Measured high resolution X-Ray diffraction curves of InGaAsBi samples grown at different temperatures

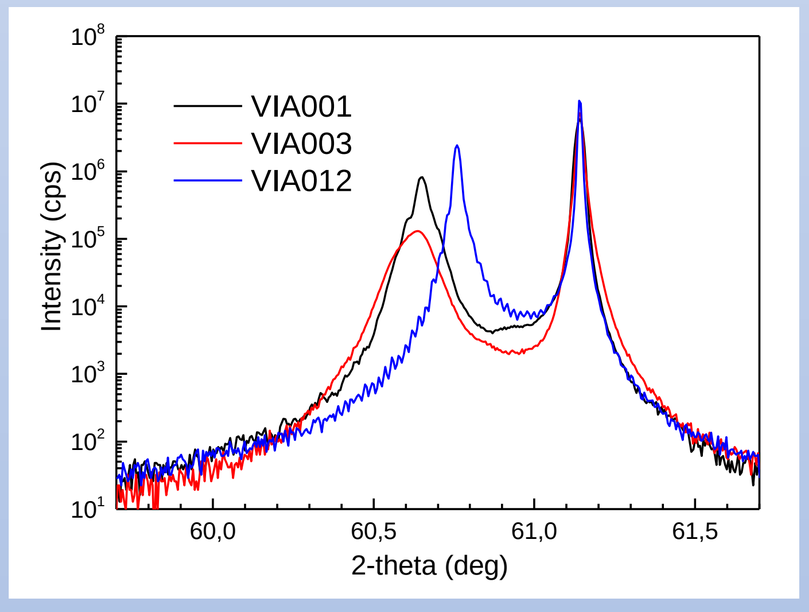

Fig. 2. XRD (004) rocking curves measured on three InAsBi samples VIA001, VIA003, and VIA012.

MBE growth of InAsBi/AlAsSb on (100) InAs substrates:
In difference with InGaAsBi/AlAsSb material system, the InAs/Al(As)Sb system is considered as nearly lattice matched to the substrate. Hence easier calibration and adjustment procedures are needed. On the other hand, this material system quite close in composition to the first one. Hence, in similarity, initial bismide growth conditions were found in the same way. The optimal growth temperature of InAsBi material has been determined by the As cap desorption temperature, which occurs at nearly 300 ˚C. Each substrate prior to be loaded into the growth chamber has been outgassed at 200 ℃ in the load lock and later at 300 ℃ in the buffer chamber. The native oxide removal was performed at 525 – 530 ℃ temperature according to the pyrometer readings and under ~1×105 Torr beam equivalent pressure (BEP) As_2 flux. After that the substrate temperature was decreased to 500 – 515 ℃ for InAs buffer layer growth. RHEED oscillation measurements were performed to estimate the growth rate of InAs and III/V ratios prior to the growth of InAsBi layers. InAsBi layers in all samples were grown at 320 ℃ temperature according to the thermocouple readings. Thicknesses of below presented grown InAsBi layers in samples VIA001, VIA003, VIA012 are respectively 390 nm, 400 nm, and 500 nm. All the samples were grown at the 0.5 monolayer/s growth rate. The bismuth content in InAsBi layers was determined from the X-ray diffraction (XRD) (004) rocking curves. XRD traces obtained on all three InAsBi samples are presented in Figure 5. Flattened top of InAsBi peak of VIA012 suggests the possible layer relaxation due to higher bismuth concentration. To prove that (115) Reciprocal Space Maps (RSM) of two InAsBi samples with the largest 2θ shifts from the substrate were registered and are presented in Figure 6. Two strong peaks can be clearly distinguished on these maps: the upper peak can be associated with the InP substrate, the lower one with the InAsBi layer, red lines on the maps correspond to fully strained and fully relaxed states and the blue line shows different relaxation states with the same Bi content. It can be seen from this figure that InAsBi layer with lower Bi content (Fig. 6a) grown on InAs substrate is strained, whereas InAsBi layers with higher Bi content have a relaxation level of 40%. The composition of all InAsBi layers and other parameters are given in Table 1.

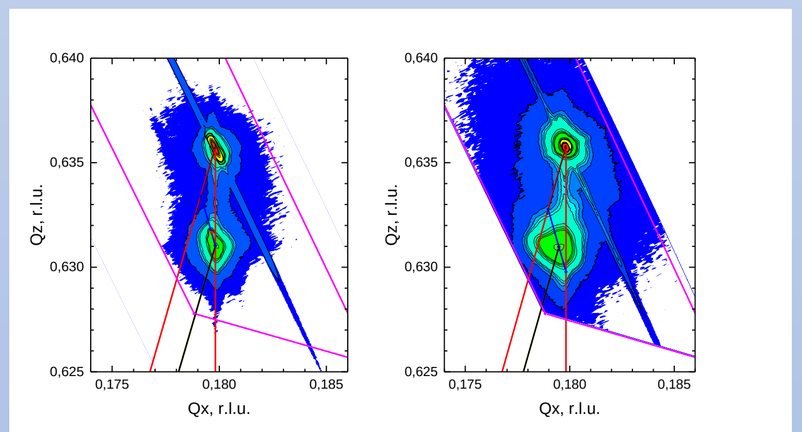

Fig. 3. Reciprocal Space Maps (RSM) of two InAsBi samples: VIA003 (a) and VIA012 (b). The red lines on the maps correspond to fully strained and fully relaxed lattice states and the blue line indicates the states with the same Bi content and different relaxation levels.

Sample	Bi concentration, %	Relaxation, %	Thickness, nm
VIA012	2.7	0%	390
VIA001	3.6	0%	400
VIA003	4.55	40%	480

Table 1. Main parameters of the investigated samples.

Conclusions:
The MBE growth technique for the epitaxy of InAsBi/Al(As)Sb and InGaAs/AlAsSb quantum wells has been developed. Bismuth containing superlattices exhibited excellent interface contrast and crystalline quality. Obtained growth conditions can be considered as suitable for the growth of Bismide-based intersubband devices. Measured intervalley scattering confirmed that incorporation of Bi into the quantum well can reduce carrier escape to lateral valley.
Using developed growth technique and optimized growth conditions the InAsBi/AlAsSb intersubband emission structure has been grown. The electroluminescence spectrum has been obtained from fabricated EL structure. Emission wavelength peak in vicinity of 3.3 µm has been recorded. This confirmed that there is no degradation in performance associated with insertion of Bi and further design modifications are possible to exploit advantage of Bi in quantum wells for development of short wavelength intersubband devices.

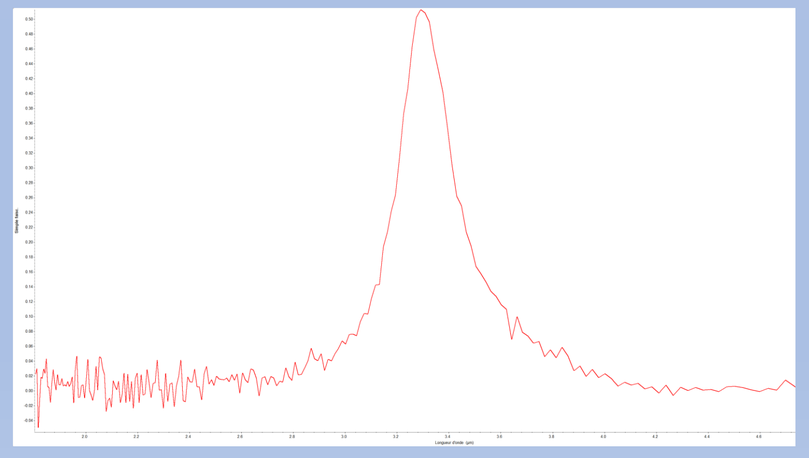

Fig. 4. EL emission spectrum obtained from InAsBi/Al(As)Sb sample.

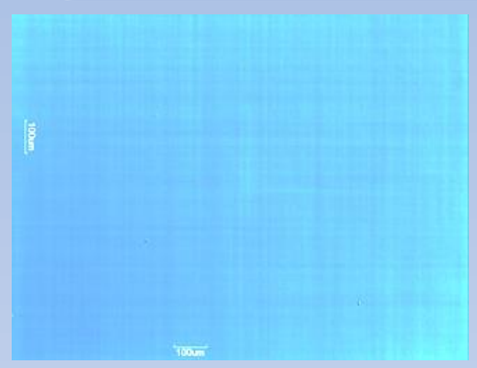

Fig. 5. Nomarski microscope image of the surface of the sample grown using only interface alteration technique ←

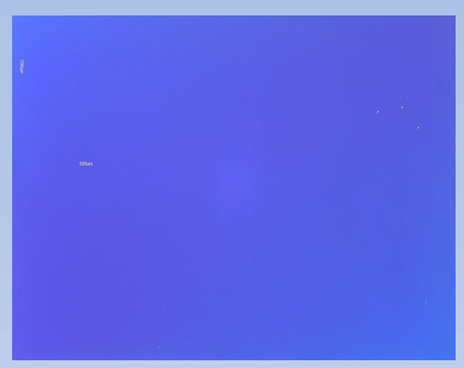

Fig. 6. Nomarski microscope image of the surface of the optimized InAs/Al(As)Sb sample grown using lattice matching technique. ←

Sources:
[1] R Butkute, A Geižutis, V Pačebutas. B Čechavičius, V Bukauskas, V Kondrotas, P Ludewig, K Volz, A Krotkus; Electronics Letters. 50. 1155–1157. 10.1049/el.2014.1741, 2014
[2] K. Alberi, J. Wu, W. Walukiewicz, K. M. Yu, O. D. Dubon, S. P. Watkins, C. X. Wang, X. Liu, Y.- J. Cho, and J. Furdyna.;. Phys. Rev. B, 75:045203, 2007
[3] J. Devenson. InAs/AlSb SHORT WAVELENGTH QUANTUM CASCADE LASERS. Dissertation, 2010.

CENTER FOR PHYSICAL SCIENCES AND TECHNOLOGY

APROPOS 17, Vilnius, Lithuania 2020/09/30

Determination of electron drift velocity from hot-electron effect in ZnO epilayers and AlGaN/AlN/GaN heterostructures

Oleg Kiprijanovič and Linas Ardaravičius

Email:linas.ardaravicius@ftmc.lt

Drift velocity, gate length, and cut-off frequency in FET

Effective carrier saturation velocity in a field-effect transistor

L_g – gate length

f_T – current gain cut-off frequency

$$v_s = 2\pi f_T L_g$$

Carrier drift velocity and Pulsed dc technique

$$v_d = \frac{I}{enw}$$

I - current, e – elementary charge, n – carrier density, w- sample cross section area (width)

AlGaN/GaN HEMT: A. Vertiatchikh et al., WOCSDICE (2003) & ISCS (2003) **DOI:** 10.1109/ISCSPC.2003.1354444 v_s = 1.1x10^7 cm/s; ZnO FET: S. Sasa et al., Phys. Stat. Sol. A **208,** 449 (2011); f_T = 1.75 GHz

Maximum electron drift velocity in ZnO

The highest experimental electron velocity value is close to the peak value obtained by Monte Carlo simulation [1]. Highest experimental room temperature electron drift velocity in nominally undoped ZnO at 320 kV/cm: v_{dmax} = 2.7±0.3x10^7 cm/s [2]. Electrical pulses of few nanoseconds (3 ns) in duration were used. Experimental results up to moderate electric fields are in good agreement with theoretical calculations by spherical harmonics expansion (SHE) method.

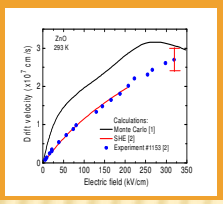

[1] J. D. Albrecht, P. P. Ruden, S. Limpijumnong, W. R. L. Lambrecht, and K. F. Brennan, J. Appl. Phys **86**, 6864 (1999).
[2] L. Ardaravičius, O. Kiprijanovič, M. Ramonas, E. Šermukšnis, J. Liberis, A. Šimukovič, A. Matulionis, Md. B. Ullah, K. Ding, V. Avrutin, Ü. Özgür, and H. Morkoç, J. Appl. Phys. **126**, 185703 (2019).

Electron density $n_0 = \sigma_0/e\mu_0$ = 1.9x10^{17} cm^{-3} (circles);1x10^{17} cm^{-3} (solid lines [1]).

Differential mobility, conductivity, and effective defect density

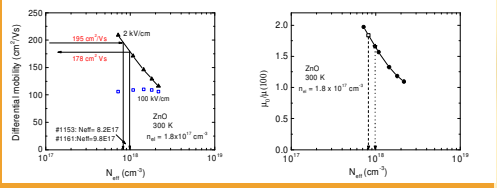

Calculated differential mobility ratio at low (2 kV/cm) and moderate (100 kV/cm) electric fields, $\mu_0/\mu(100)$, versus the total charged defect density N_{eff} is compared with the ratio of conductivities, $\sigma_0/\sigma(E_m)$, obtained from the experiment [4]:

$$\frac{\mu_0}{\mu(E_m)} = \frac{\sigma_0}{\sigma(E_m)} = 1.84$$

Drift velocity in AlGaN/AlN/GaN and ZnO

For higher low-field electron mobility (1880 cm^2/(Vs)) AlN-spacer containing structure electron drift velocity saturates and attains the value of 1.6 x10^7 at 95 kV/cm. The highest electric field reached is 140 kV/cm. At this particular field, both drift velocity values in epitaxial ZnO and 2DEG GaN channel are similar.

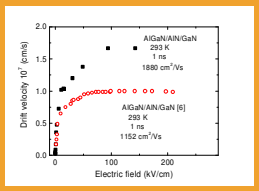

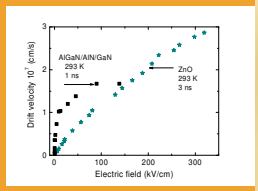

[6] L. Ardaravičius, A. Matulionis, J. Liberis, O. Kiprijanovic, M. Ramonas, L.F. Eastman, X. Chen, Sun Yun-Ju, *Physica Status Solidi (a)*, vol. **202** , 808-811, 2005.

Zinc oxide (ZnO) is a semiconductor with a direct and relatively wide bandgap. High electron drift velocity saturation (3.2 x 10^7 cm/s) was attained from Monte Carlo calculations [1] and recent experimental findings of the drift velocity (~2.7 × 10^7 cm/s at 320 kV/cm) and electric fields (430 kV/cm) were reported for nominally undoped ZnO epilayers at room temperature [2]. These results are promising to field-effect transistors (FETs) for high-frequency and high-power operations. The dependence of electron drift velocity on the electron density was deduced at room temperature for doped ZnO [3].

The electron low-field mobility in ZnO is mainly determined by scattering on charged defects. There is an experimental evidence that double charged oxygen vacancies act as shallow donors and charged scattering centres. The goal of this work is to examine the electron scattering by charged defects through the study of hot-electron effects in nominally undoped ZnO epilayers at room temperature. The current–voltage dependence is measured up to high electric fields, and the experimental results are fitted with the solution of the Boltzmann kinetic equation [4]. The results are used for the estimation of electron density, drift velocity and low-field mobility. The electron scattering by the double-charged oxygen vacancies and other charged defects is discussed.

As a promising candidate for future high-electron-mobility transistors (HEMTs) used in microwave high-power applications, GaN-based heterostructure two-dimensional electron gas (2DEG) channels have attracted much interest [5]. The insertion of a thin AlN spacer layer prevents electron penetration into adjacent AlGaN layer and simultaneously improves the sheet charge density and mobility compared with the conventional AlGaN/GaN heterostructure having equivalent AlGaN parameters. Our goal is to extract the key transport parameter – the electron drift velocity.

[3] L. Ardaravičius, O. Kiprijanovič, J. Liberis, M. Ramonas, E. Šermukšnis, A. Matulionis, M. Toporkov, V. Avrutin, U. Özgur, and H. Morkoç, *Mater. Res. Express* **4**, 066301 (2017).
[5] A.S.A. Fletcher and D. Nirmal, Superlattices and Microstructures **109,** 519-537 (2017).

Intentionally undoped ZnO samples

The investigated epitaxial ZnO layers were grown in Virginia Commonwealth university (USA) by (PA-MBE) on highly-resistive GaN prepared by MOCVD on c-plane sapphire. ZnO epilayer width w = 300 µm and thickness d = 350-375 nm. The transmission line measurement (TLM) patterns were processed with evaporated Ti/Au (25 nm/30 nm) stacks acting as ohmic contacts. The contact resistance (R_c = 23±10Ω) was estimated at low electric fields from the dependence of the sample resistance on the inter-electrode distance (L = 1.7-15.8 µm). The channel resistance, the length and the cross section area were used to estimate the low-field conductivity. Electron mobility in the channel was estimated from Hall effect and magnetoresistance measurement data. More oxygen-rich conditions as well as lower substrate temperature during the growth (340° C) gave rise to lower electron density.

Sample	#1153(#1161)
Epilayer conductivity σ_0	4.7(5.5) S/cm
Magnetoresistance electron mobility	188(146) cm^2/(Vs)
Electron drift mobility μ_0	195(178) cm^2/(Vs)
Electron density n_0	1.5(1.9)x10^{17} cm^{-3}
Hall electron mobility	53(50) cm^2/(Vs)
Oxygen vacancy density	1.6(1.9)x10^{17} cm^{-3}
Other charged defect density	1.7(2.0)x10^{17} cm^{-3}

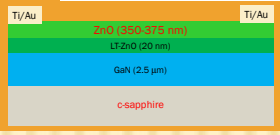

$$n(E_m) = \frac{\sigma(E_m)}{e\mu(E_m)} = n_0 = \frac{\sigma_0}{e\mu_0}$$

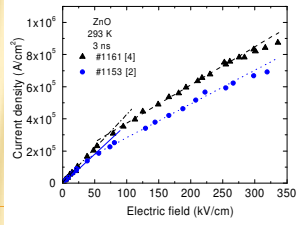

Experimental current density-electric field (*j-E*) results for ZnO can be approximated with lines:
E < 50 kV/cm: A solid line and dashed dotted lines stand for the Ohm's law.
50 kV/cm < E = E_m < 250 kV/cm: Dashed and dotted lines with a lower slope illustrates the second Ohm's law
$\sigma(E_m)$ - differential conductivity at E_m can be found from the slope of *j-E* curve:

$$\sigma(E_m) = \frac{dj}{dE}(E_m)$$

AlGaN/AlN/GaN 2DEG channel

The heterostructures were grown in Virginia Commonwealth university (USA) by MOCVD on c-sapphire substrates. The 2DEG channel formed in the top-most portion of 3.2 µm-thick GaN layer. Transmission-line measurement (TLM) patterns with mesa etching were fabricated with the electrode dimensions of 300x80 µm^2 and the gaps from 3 to 27 µm. The magnetoresistance measurements were performed on the TLM structures. The contact resistance R_c was evaluated from the TLM length-dependent resistance measurements; the values were found to be much lower compared to the resistance of the 6.9 µm length channel. The Hall mobility and the TLM-evaluated resistance value were also utilized simultaneously for estimation of the sheet 2DEG density.

Sample	#4338
Channel conductivity σ_0	1.6 mS
Magnetoresistance electron mobility	1700 cm^2/(Vs)
Hall sheet electron density	8.6x10^{12} cm^{-2}
TLM sheet electron density	5.2x10^{12} cm^{-2}
Hall electron mobility	1880 cm^2/(Vs)

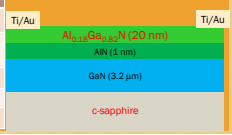

Experimental setup for measurements of sub-nanosecond pulsed current-voltage (I-U) dependence

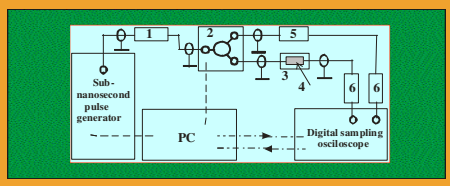

1 - high-voltage attenuator, 2 - wide-band switch, 3 - sample holder, 4 - sample under test, 5 - reference resistor, 6 - tunable wide-band attenuator.

L. Ardaravičius, O. Kiprijanovič, J. Liberis, A. Matulionis, E. Šermukšnis, R. A. Ferreyra, V. Avrutin, Ü. Özgür, and H. Morkoç, *Semicond. Sci. Technol.* **30,** 105016 (2015).

Transient current and electric field measurements

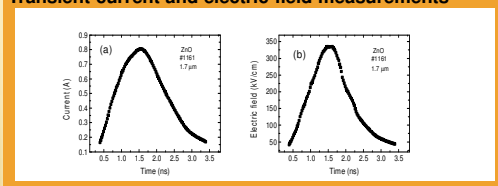

The transmitted current (a) and electric field (b) waveforms for the ZnO sample #1161. The highest current of 0.8 A corresponds to 320 kV/cm peak field at 26 dB attenuation. The current deduced during the rise edge nearly coincides with that available from the falling edge. The coincidence suggests that neither the sample temperature nor the electron density change with time and electric field.

[4] L. Ardaravičius, O. Kiprijanovič, M. Ramonas, E. Šermukšnis, A. Šimukovič, and A. Matulionis, *Lithuanian J. Phys.* **60**, 48-56 (2020).

Drift velocity in ZnO and Zn cell temperature

The highest experimental value for the electron drift velocity of ~2.9 × 10^7 cm/s (~2.7×10^7 cm/s) is found at 320 kV/cm in the sample #1153 (#1161) with the electron density of 1.5×10^{17} cm^{-3} (1.9 × 10^{17} cm^{-3}). A correlation with the growth conditions is resolved: a slightly higher drift velocity is estimated for the sample #1153 with a lower density of oxygen vacancies. This wafer has been grown at lower Zn cell temperature (340 °C). The highest drift velocity value is close to that obtained from Monte Carlo calculations [1].

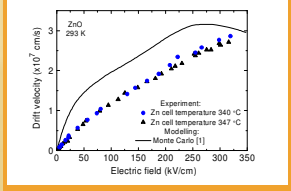

Electron density $n_0 = \sigma_0/e\mu_0 = n(E_m) = \sigma(E_m)/e\mu(E_m)$ = 1.5(1.9)x10^{17} cm^{-3} circles(triangles); 1x10^{17} cm^{-3} (solid line [1]).

Acknowledgments

Authors are thankful to Dr. E. Šermukšnis and Prof. A. Matulionis from Center for Physical Sciences and Technology, Lithuania, for discussion and Prof. H. Morkoç group at Virginia Commonwealth University (USA) for ZnO and nitride samples.

Optical properties of GeSi/Si quantum dots in mid- and far-IR range

Roman M. Balagula[1], Anton N. Sofronov[2], Hayk A. Sarkisyan[3], and Dmitry A. Firsov[2]

[1] Center for Physical Sciences and Technology, Vilnius, Lithuania
[2] Peter the Great St. Petersburg Polytechnic University, St. Petersburg, Russia
[3] Russian-Armenian University, Yerevan, Armenia

Apropos 17
Advanced Properties and Processes in Optoelectronic Materials and Systems
29 September – 01 October, 2020

1. Samples: high-density array of Ge/Si quantum dots

Sb-mediated MBE-growth

Growth temperature - 600°C
Dot material - Ge_xSi_{1-x} (x = 0.6… 0.65)
Dot surface density ≈ 2×10^{11} cm^{-2}

Doping	Holes per dot
0	0
4×10^{11} cm^{-2}	2
8×10^{11} cm^{-2}	4
1.2×10^{12} cm^{-2}	6

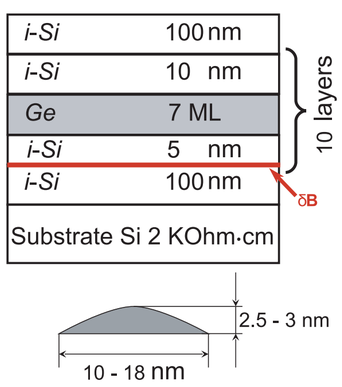

Sample geometry for optical measurements

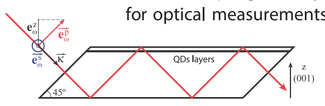

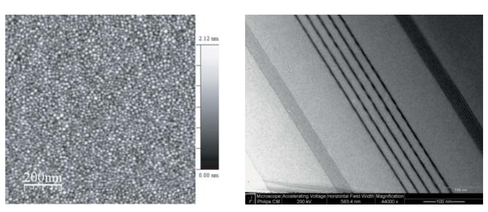

2. Mid-IR optical absorption

Equilibrium

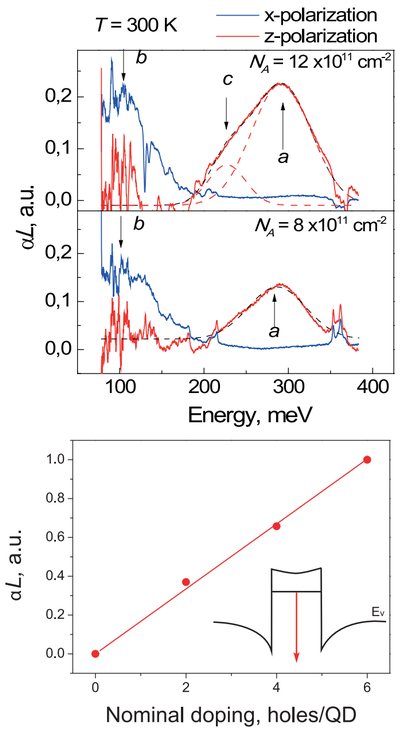

Photoinduced

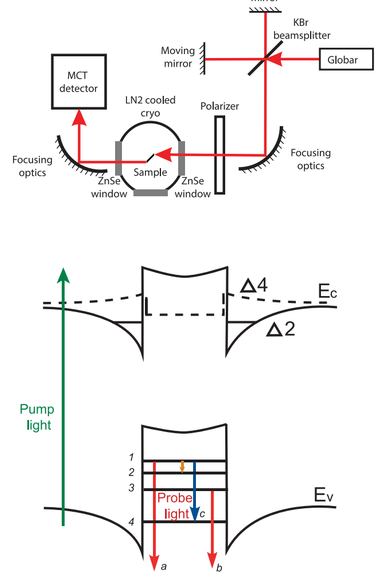

Actual average number of holes in QDs linearly follows the nominal doping.
There are positively charged QDs with more than 1 hole inside.

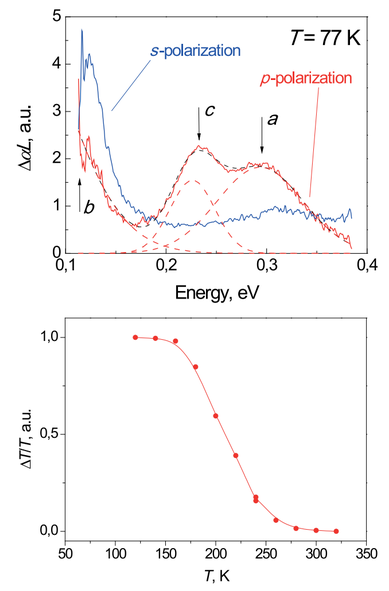

$$g(E)=\frac{N_{QD}}{L}\sum_{i=1}^{\text{all QD states}}\frac{g}{\sigma\sqrt{2\pi}}\exp\left(-\frac{(E-E_i)^2}{2\sigma^2}\right)+$$
$$+\frac{\sqrt{2}m_h^{3/2}}{\pi^2\hbar^3}\sqrt{E-E_i}\,H(E-E_i)$$

L_{eff} – is different for doped and undoped samples!
Doped structure – L_{eff} = 15 nm – distance between δ-layers.
Undoped structure – L_{eff} = 500 μm – bipolar diffusion length.

3. Far-IR optical absorption

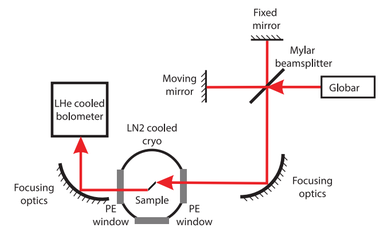

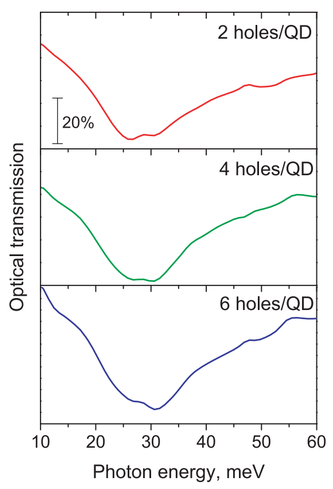

Nothing happens with the increase of the average number of holes in QDs

Energy of transitions to low excited levels does not depend on the number of holes in QDs

For multiparticle states this effect is observed in parabolic potential:
In magnetic field W. Kohn Phys. Rev. 123, 1242 (1961)
In "parabolic" QDs - P.A. Maksym, T. Chakraborty Phys. Rev. Lett. 65,108 (1990),
F.M. Peeters Phys. Rev. B 42, 1486(R) (1990)

4. Model: Lens-shaped Ge/Si QD

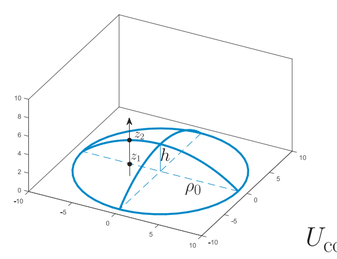

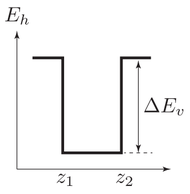

$$U_{\text{conf}}(\vec{r})=\begin{cases}0, & \text{inside},\\ \Delta E_v, & \text{outside}.\end{cases}$$

5. Where is a parabolic potential in "rectangular-band-profile" QD?

Adiabatic separation of hole motion in xy-plane and along z-axis: $\rho_0 >> h$

According to D.B. Hayrapetyan, E.M. Kazaryan, and H.A. Sarkisyan. Physica E, 75, 353 (2016)

$$\hat{H}_0\Psi+U_{\text{conf}}\Psi=\mathcal{E}\Psi \qquad \Psi(\rho,\varphi,z)=f(\vec{\rho})\chi(z(\rho))$$
$$\Delta E_v\gg\hbar\omega:$$

At fixed ρ the hole is confined along z

in 1D infinite well of width $z_2 - z_1 = a(\rho)$

$$a(\rho)=\sqrt{R^2-\rho^2}-(R-h)$$
$$\chi_n(z(\rho))=\sqrt{\frac{2}{a(\rho)}}\sin\left(\frac{\pi n}{a(\rho)}z\right)$$
$$\mathcal{E}_n^{(z)}=\frac{\pi^2\hbar^2n^2}{2m(a(\rho))^2}\equiv U_n^{\text{eff}}(\rho)$$

if $\rho<<\rho_0$: Hole confinement potential in xy – plane

$$U_n^{\text{eff}}(\rho)=\frac{\pi^2\hbar^2n^2}{2mh^2}+\frac{m\Omega_n^2}{2}\rho^2$$
$$\Omega_n^2=\frac{\pi^2\hbar^2n^2}{m^2\hbar^3R}$$

6. From single-particle to many-particle problem

$$\hat{H}(1,2,\dots N)=\sum_{j=1}^{N}\hat{H}_0^j+\sum_{j=1}^{N}U_{\text{conf}}(\vec{r}_j)+V(\vec{r}_1,\dots\vec{r}_N)$$

Adiabatic separation: $\Psi(\vec{r}_1,\dots\vec{r}_N)=f(\vec{\rho}_1,\dots\vec{\rho}_N)\chi_{n_1,\dots n_N}(z_1(\rho_1),\dots z_N(\rho_N))$

$$n_1=\dots=n_N=1$$
$$V=\frac{1}{2}\sum_{\substack{i,j=1\\ i\neq j}}^{N}\frac{e^2}{\varepsilon|\vec{\rho}_i-\vec{\rho}_j|} \qquad \hat{H}^{2D}=\frac{1}{2m}\sum_{j=1}^{N}\left(\hat{P}_{xj}^2+\hat{P}_{yj}^2\right)+\frac{m\Omega_2}{2}\sum_{j=1}^{N}\rho_j^2+\frac{1}{2}\sum_{\substack{i,j=1\\ i\neq j}}^{N}\frac{e^2}{\varepsilon|\vec{\rho}_i-\vec{\rho}_j|}$$

Changing variables from ρ_j to CM motion and relative motion of the particles:

$$\vec{R}_{\text{CM}}=\frac{1}{\sqrt{N}}\sum_{j=1}^{N}\vec{\rho}_j \qquad \hat{H}^{2D}=\hat{H}_{\text{CM}}^{2D}+\hat{H}_{\text{Rel}}^{2D}=-\frac{\hbar^2}{2M}\frac{d^2}{dR_{\text{CM}}^2}+\frac{M\Omega^2}{2}R_{\text{CM}}^2+\hat{H}_{\text{Rel}}^{2D}$$

The EM wave perturbation operator in dipole approximation

$\Delta\hat{H}=e\vec{E}(t)\sum_j\vec{\rho}_j=\sqrt{N}e\vec{E}(t)\vec{R}_{\text{CM}}$ depends on only CM coordinate.

Single-particle-like optical transitions in many-particle system are observed.

Optical absorption at the lowest intelevel resonance does not depend on the Coulomb interaction and number of holes inside the QD.

Transition energy $\hbar\Omega=\frac{\pi\hbar^2}{m\sqrt{\hbar^3R}}$

For the largest QDs in ensemble h ≈ 2.95 nm, ρ_0 ≈ 9 nm, and $\hbar\Omega$ ≈ 31 meV

7. Far-IR optical absorption at higher temperatures

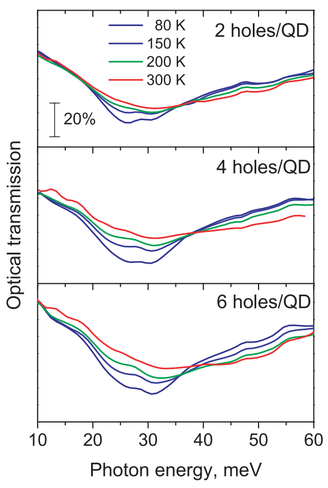

Redistribution of the holes over the smaller QDs in ensemble depends on the nominal doping

8. Mid-IR photoinduced absorption dynamics

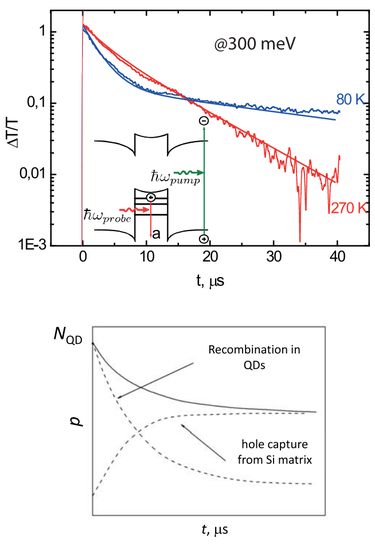

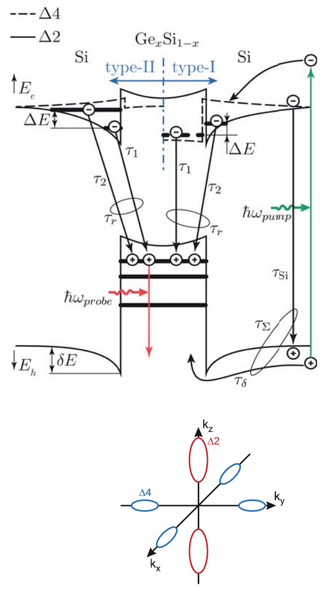

Si/Ge_xSi_{1-x}(x < 0.82)

- strain splits Δ-valleys
- δ-doping

$$p(t,T)=C_1\exp\left(-\frac{t}{\tau_r(T)}\right)+C_2\exp\left(-\frac{t}{\tau_\Sigma(T)}\right)$$
$$\tau_\Sigma^{-1}=\tau_{Si}^{-1}+\tau_\delta^{-1}$$
$$\tau_\delta^{-1}=\gamma\frac{N_{QD}-p}{l_{QD}}$$
$$\tau_r^{-1}=\tau_1^{-1}(1+\exp(-\Delta\varepsilon/k_BT))^{-1}+\tau_2^{-1}(1+\exp(-\Delta\varepsilon/k_BT))^{-1}$$

From temperature dependences of characteristic times we find ΔE = 25 meV and δE = 70 meV

Conclusions

1. Equilibrium and photoinduced absorption in GeSi QDs related to intersubband hole transitions are investigated.

2. The effect of thermal depopulation of the GeSi/Si quantum dots at temperatures below 300 K is observed in photoinduced absorption of undoped samples when the bipolar diffusion of charge carriers is not restricted.

2. Equilibrium absorption depends on doping differently in mid-IR and FIR optical regions.

3. Kohn's theorem applicability to such structures was experimentally shown.
   - There is a certain energy range where the motion of the holes in Ge/Si quantum dots is equivalent to the motion of 2D particles in parabolic potential.
   - The analytical size-quantization theory developed for holes in Ge/Si QDs on the basis of the adiabatic approximation gives good agreement with the experimental energy of the lower intraband resonance.
   - The resonance frequency does not depend on the interaction between holes and is of a single-particle character.
   - The conditions for generalized Kohn's theorem are satisfied due to the specific geometric shape of the QDs.

4. The existence of potential barrier for holes at the heterointerface and its influence on optical properties was experimentally proven.

5. First investigation of photoinduced absorption dynamics in QD structures was performed. Two stage behavior of absorption relaxation is qualitatively explained.

e-mail:roman.balagula@ftmc.lt

P2-1

In-situ SHINERS analysis of SAM from thiols with imidazole ring and intrachain amide groups

Agnė Zdaniauskienė[1], Tatjana Charkova[1], Rita Sadzevičienė[1], Gediminas Niaura[1]

[1]*Department of Organic Chemistry, Center for Physical Sciences and Technology, Saulėtekio Ave. 3, LT-10257 Vilnius, Lithuania*
Email: agne.zdaniauskiene@ftmc.lt

The self-assembled monolayers (SAMs) constructed by the adsorbtion of thiols on noble metals are widely used to analyze the interaction of functional groups with adsorbates, study electron transfer processes and develop bioelectronic devices [1].

Introduction of amide functionality in the hydrocarbon chain of adsorbing molecules considerably increases the stability of the formed SAMs due to the formation of hydrogen bonds between the adjacent molecular chains in the monolayer [2]. A terminal histidine (His) ring group containing monolayers provide a possibility to study various interactions of the ring with solution components. The unique structure of His makes it play multiple roles in the molecular interactions - it is an important ligand for metal coordination in peptides and proteins [3].

Shell-isolated nanoparticle-enhanced Raman spectroscopy (SHINERS) method employs the ultrathin shell to isolate the metal nanospheres from the probed object and thus prevents a potentially disturbing interaction. Meanwhile, the very short metal–molecule separation can still result in a significant nanoparticle-enhanced Raman signal [4].

The present work focused on *in situ* SHINERS study of SAM formed from N-(2-(1H-imidazol-4-yl)ethyl)-6-mercaptohexanamide (IMHA) at smooth Au surface in aqueous solutions. SHINERS method employing synthesized spherical Ag nanoparticles with 85 ± 5 nm core size and SiO_2 shell of 3 nm thickness allowed to obtain significantly enhanced SHINERS spectrum of IMHA compared to the Raman spectrum (Fig. 1). Bands from all parts (terminal imidazole ring, hydrocarbon chain, and sulfur group) of IMHA are clearly visible.

Therefore, it was shown that SHINERS is a perspective technique allowing the collection of molecular level information from smooth Au surface for a better understanding of molecular structures and functions.

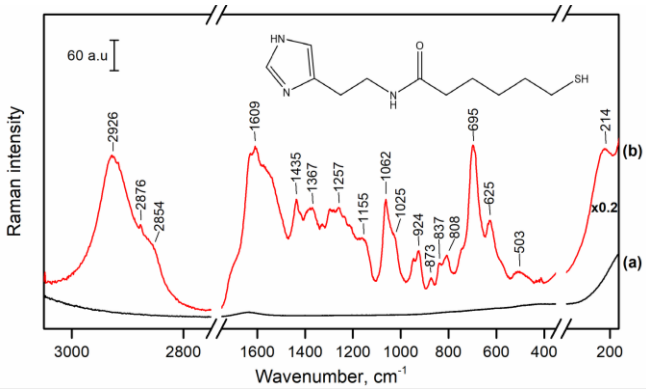

Fig. 1 Raman spectrum of IMHA adsorbed on smooth Au surface **(a)** and SHINERS spectrum from smooth Au surface with adsorbed IMHA **(b).**

REFERENCES

[1] J. C. Love, L. A. Estroff, J. K. Kriebel, R. G. Nuzzo, G. M. Whitesides; *Chem. Rev.* **105** (2005) pp. 1103–1170.
[2] M. Kim, J. N. Hohman, A. C. Serino, P. S. Weiss; *J. Phys. Chem. C* **114** (2010) pp. 19744–19751.
[3] S. M. Liao, Q. S. Du, J. Z. Meng, Z. W. Pang, R. B. Huang; *Chem. Cent. J.* **7** (2013).
[4] J.R. Anema, J.F. Li, Z.L. Yang, Ren B, Z.Q. Tian; *Annu. Rev. Anal. Chem.* **4** (2011) pp. 129–150.

Polarity sensors based on thiophene-substituted BODIPY molecular rotors

CENTER FOR PHYSICAL SCIENCES AND TECHNOLOGY

Vilnius University

Karolina Maleckaitė[1], Jelena Dodonova[2], Sigitas Tumkevičius[2], Aurimas Vyšniauskas[1]

karolina.maleckaite@ftmc.lt

Background

• Easy way to image viscosity is provided by viscosity-sensitive fluorophores - **molecular rotors.** [1]

• **BODIPY based** molecular rotors are very promising because of their easy functionalization, high molar extinction coefficients, monoexponential fluorescence lifetime and photostability. [2]

• A recent research has showed that attached **thiophene moieties** to the BODIPY core **can rotate** and this suggests that these derivatives **could be sensitive to viscosity**. [3]

• In this work two **thiophene-substituted** BODIPY molecular rotors with (**BDP-N**) and without (**BDP-T**) -NO_2 group are investigated.

BODIPY

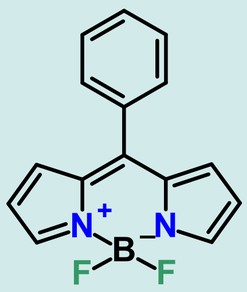

R =

-H **BDP-T**

-NO_2 **BDP-N**

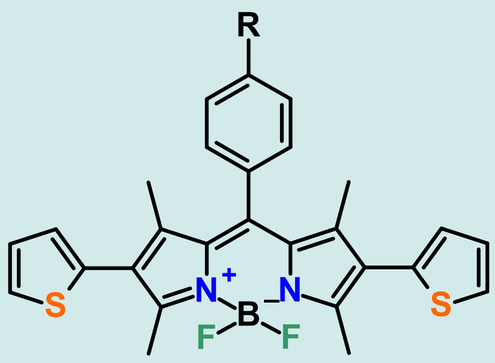

Thiophene impact

• Attaching thiophene moieties to BODIPY increases the conjugated system.

• Longer, **more biocompatible wavelengths** are achieved as well as a **larger Stokes shift** in contrast to BODIPY.

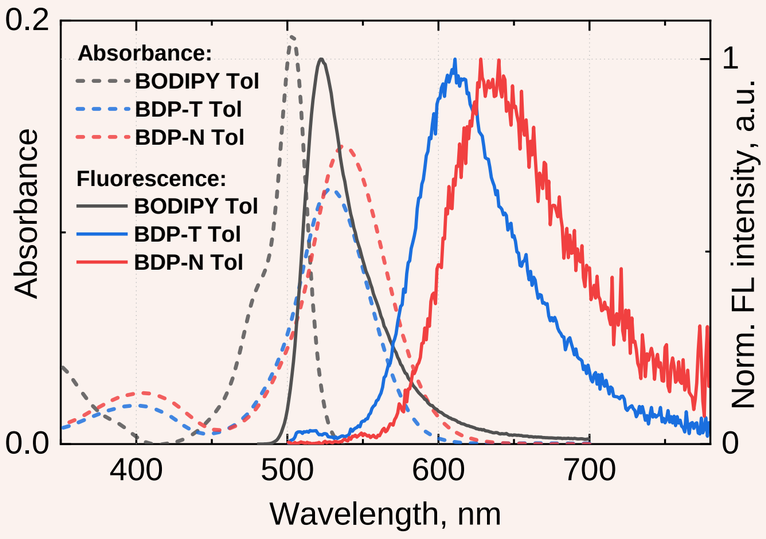

Viscosity impact

• Fluorescence spectroscopy measurements show negligible distinction between lifetimes when solvent viscosity is increased.

• **BDP-T and BDP-N derivatives cannot be used as microviscosity sensors**.

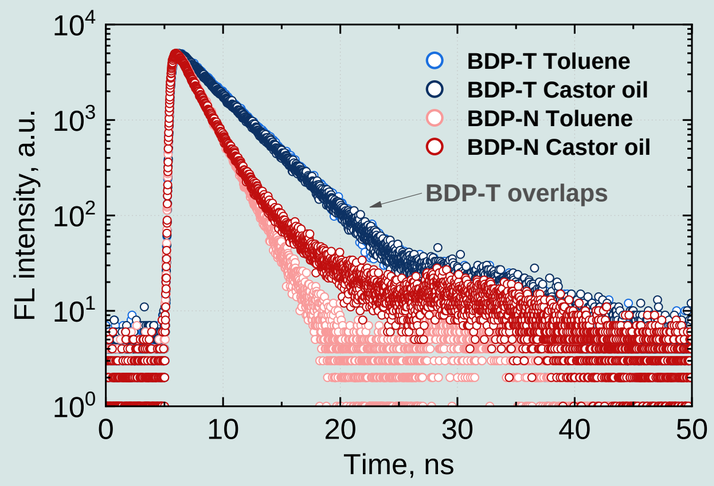

Temperature impact

• **BDP-T** and **BDP-N** dissolved in cyclohexane and **BDP-T** in chloroform showed decreasing FL lifetime with increasing temperature.

• Reverse dependence is seen for **BDP-N** in chloroform.

• **The studied derivatives are not temperature sensors.**

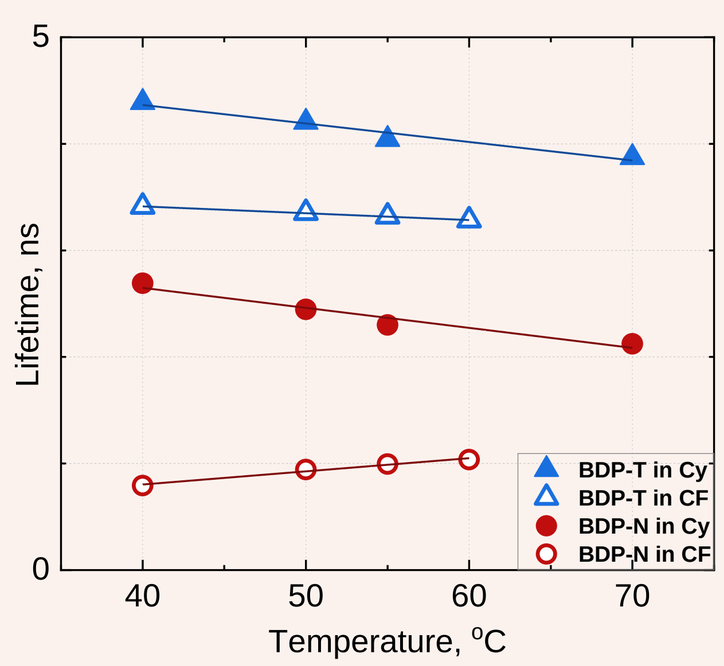

Orientation polarisability

Lippert's equation was used to rank pure solvents by their polarity.

$$\Delta f = \frac{\varepsilon - 1}{2\varepsilon + 1} - \frac{n^2 - 1}{2n^2 + 1}$$

Here ε is a relative permittivity and n is the refractive index of a pure solvent.

Polarity impact

• **Increasing orientation polarization** of the solvent (Δf) **decreases fluorescence's intensity, lifetime and quantum yield** for both studied molecules.

• Sensor sensitivity evaluation (a relative change of FL lifetime, when Δf changes by 0.1) shows that **BDP-N is more sensitive to polarity** than **BDP-T** (31% and 22%, respectively).

• **BDP-T and BDP-N can be used as polarity sensors.**

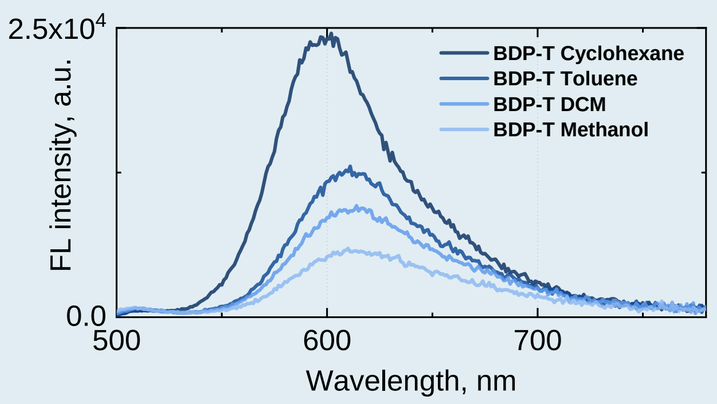

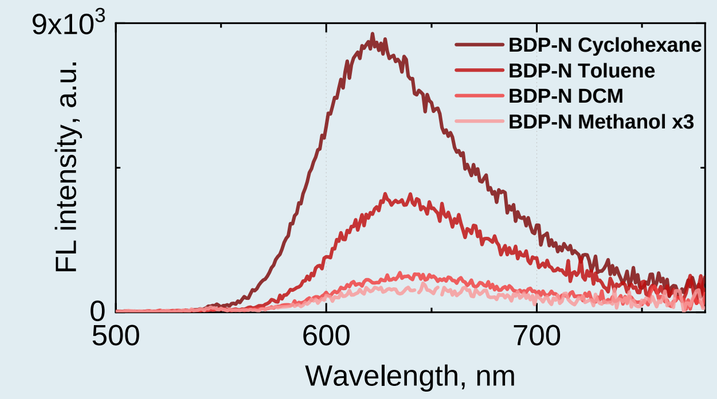

Sol-vent	Quantum yield	
	BDP-T	BDP-N
Cy	39.26 %	14.18 %
MeOH	8.66 %	1.14 %

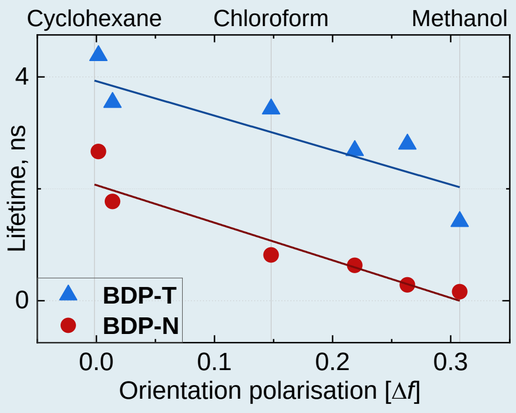

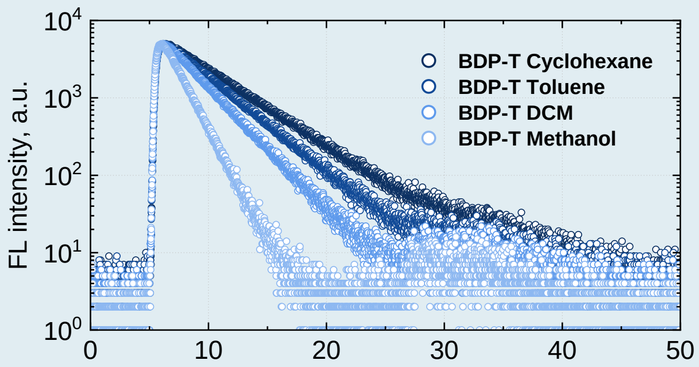

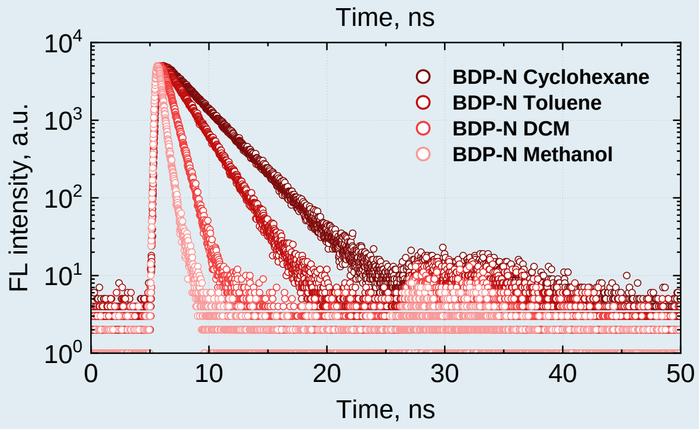

Conclusions

• Adding thiophene moieties in 2- and 6- BODIPY positions increases molecule's conjugation, redshifts fluorescent spectra and enables to achieve large Stokes shift. Furthermore, a transformation of viscosity sensor to polarity sensor is achieved.

• Fluorescence decays of **BDP-T** and **BDP-N** are monoexponential, which simplifies data analysis and reduces photon counts required for measurements.

• It is possible to create a polarity probe based on these molecules, especially **BDP-N**, which is more sensitive to solvent polarity than **BDP-T**.

References

[1] M. K. Kuimova, Phys. Chem. Chem. Phys. vol 14, no 37, p. 12671, 2012.
[2] S. Toliautas et al., Chem. Eur. J., vol. 25, 44, p. 10342-10349, 2019.
[3] Y. Chen et al., J. Org. Chem. vol. 77, 5, p. 2192-2206, 2012.

[1] Center for Physical Sciences and Technology, Saulėtekio av. 3, Vilnius, Lithuania
[2] Institute of Chemistry, Faculty of Chemistry and Geosciences, Vilnius University, Naugarduko str. 24, Vilnius, Lithuania

Energy Barriers in $MAPbI_3$ Perovskite Films

CENTER FOR PHYSICAL SCIENCES AND TECHNOLOGY

Rokas Gegevičius, Rokas Jasiūnas, Marius Franckevičius, Vidmantas Gulbinas

Molecular Compound Physics Department, Centre for Physical Sciences and Technology, Saulėtekio Ave. 3, LT-10257 Vilnius, Lithuania.

- In this work, **Transient Photocurrent**, **Time-Delayed Collection Field** and **Transient Fluorescence** techniques are combined to address charge carrier trapping processes during their lateral motion in prototypical methylammonium lead iodide perovskite ($MAPbI_3$) films formed on interdigitated electrodes.
- Carrier mobility decreases on hundreds of ns timescale, and its rate depends on the motion character—it is faster when charge carriers drift in the electric field and slower when the motion is caused by diffusion only. This difference becomes particularly evident at low temperatures. Based on the time-delayed collection field data and carrier motion modelling results, it is demonstrated that the rapid mobility decay at low temperatures is mainly caused by the energy barriers, most likely formed at crystallite boundaries.
- **Suggested concept of the potential barriers moves beyond the conventional understanding of carrier mobility, diffusion, and recombination processes in hybrid perovskites.**

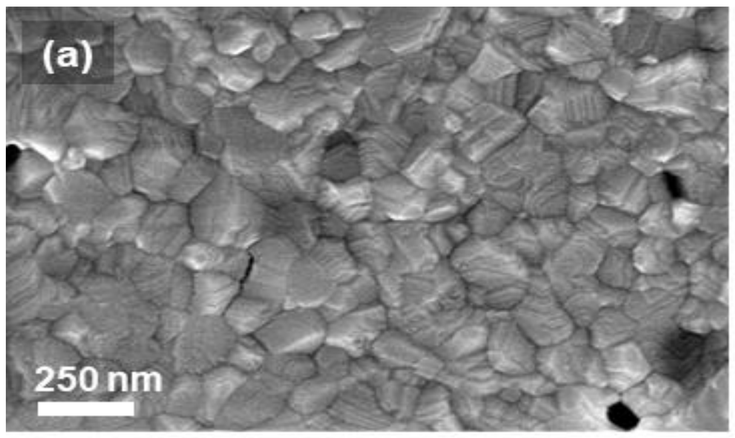

Figure 1. a) Top view scanning electron microscope (SEM) images of $MAPbI_3$ and b) The cross-sectional SEM image demonstrates lateral configurations of the perovskite films deposited on IDE.

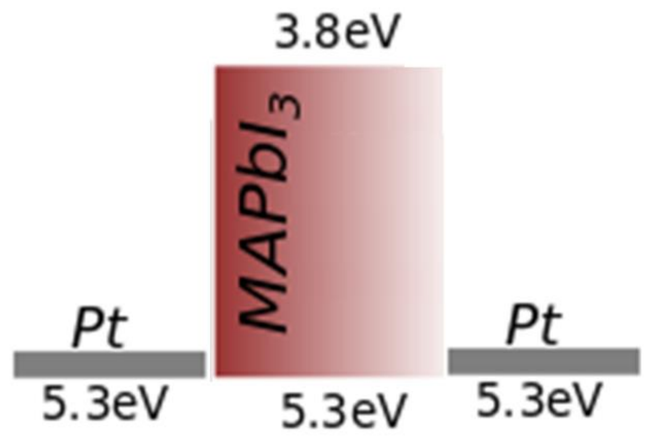

Figure 2. Energy level diagram of used samples

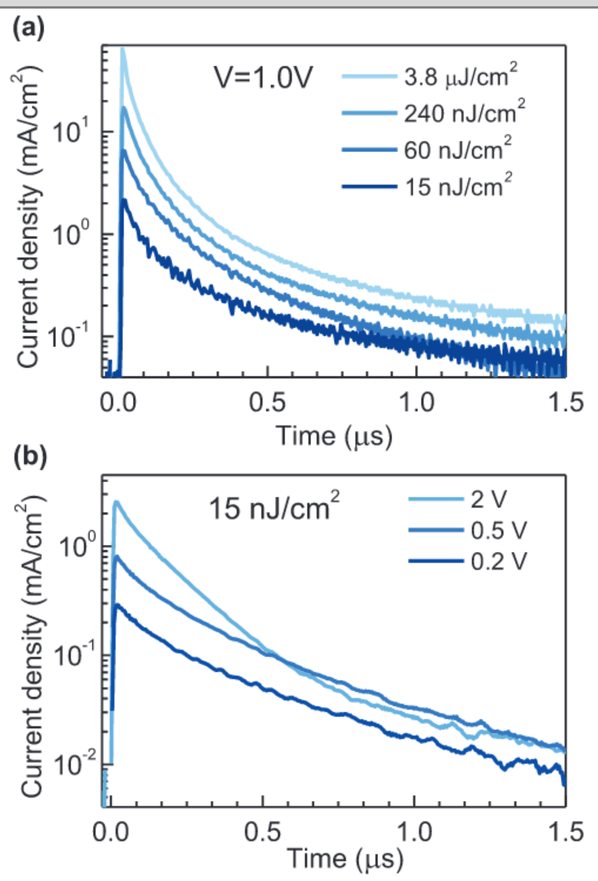

Figure 3. Transient photocurrent kinetics a) at different excitation intensities and b) at constant excitation intensity of 15 nJ cm^{-2}

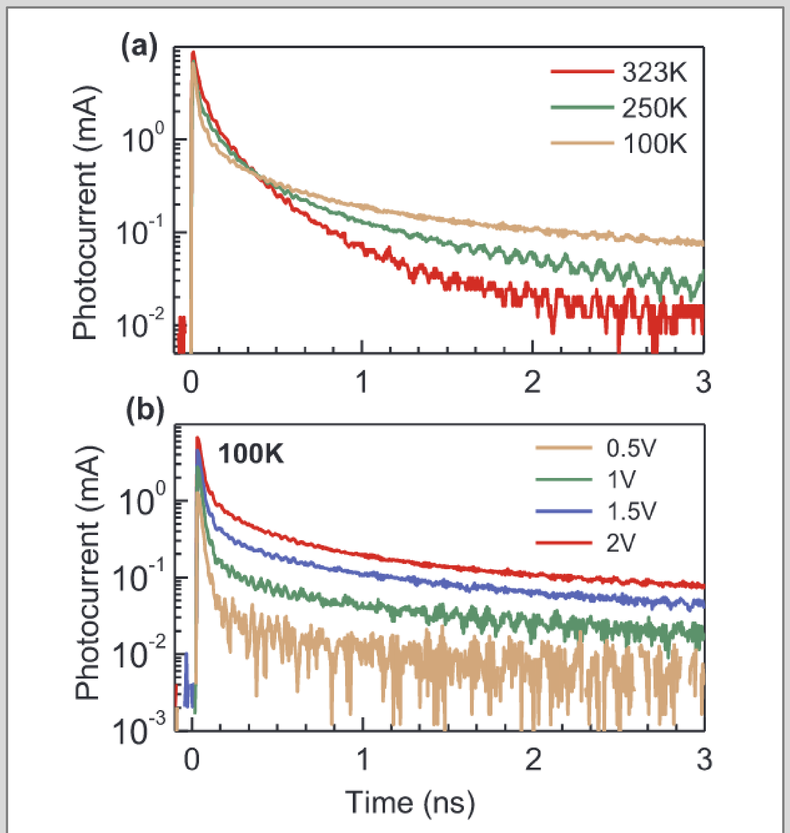

Figure 4. a) Photocurrent kinetics at different temperatures measured at 2 V applied voltage and 15 nJcm^{-2} excitation intensity, b) photocurrent kinetics at 100 K at different applied voltages.

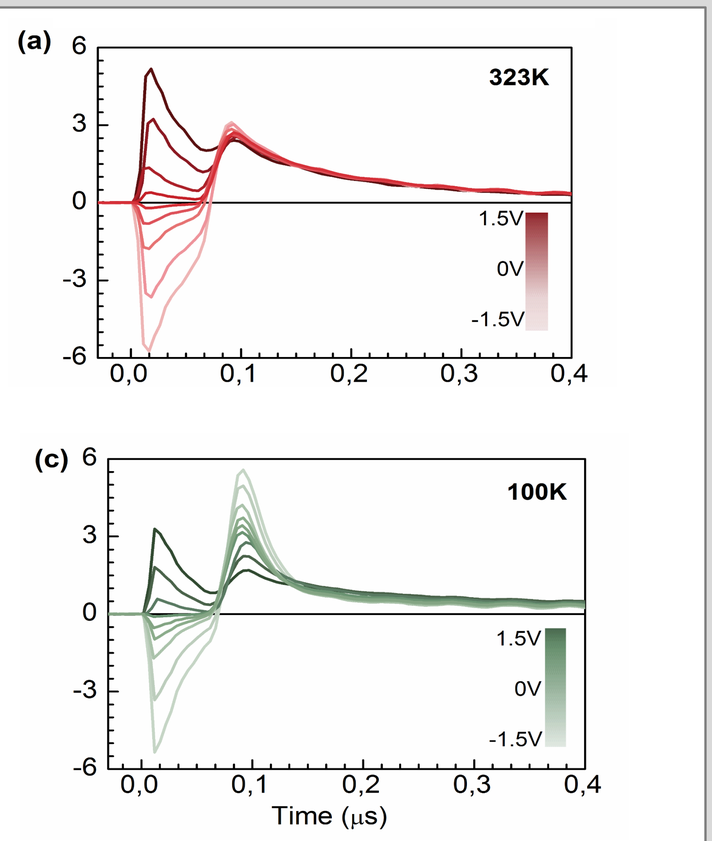

Figure 5. Photocurrent kinetics at different temperatures obtained by modified TDCF measurements under 15 nJ cm^{-2} excitation intensity.

SCAN ME

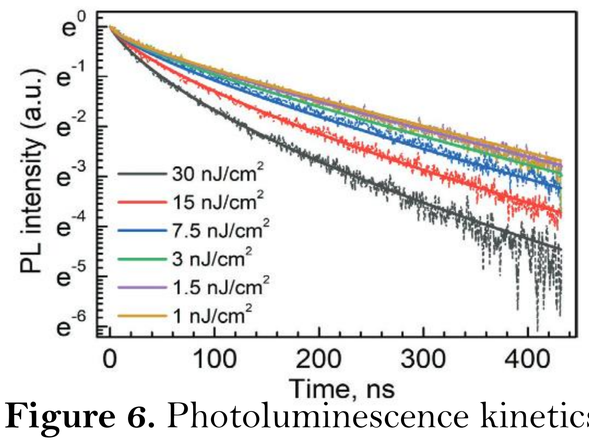

Figure 6. Photoluminescence kinetics of MAPI perovskite at different excitation intensities. λ_{ex}= 470 nm

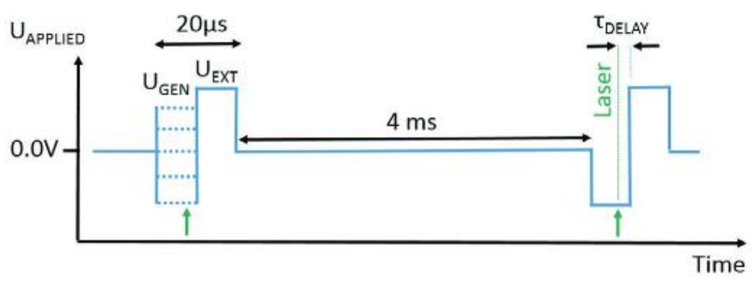

Figure 7. Time chart of the TDCF measurements. Conventional TDFC measurements correspond to Ugen= 0, while flipped field measurements were performed at Ugen< 0.

Benefits of $MAPbI_3$ perovskite doping by Sr^{2+}

Rokas Jasiūnas[1] , Rokas Gegevičius[1], Marius Franckevičius[1], Nga Phung[2], Antonio Abate[2] and Vidmantas Gulbinas[1]

[1]*Department of Molecular Compound Physics, Center for Physical Sciences and Technology, Saulėtekio Avenue 3, LT-10257 Vilnius, Lithuania.*

[2] *Helmholtz-Zentrum Berlin für Materialien und Energie GmbH, Kekuléstr. 5, Berlin D-12489, Germany.*

rokas.jasiunas@ftmc.lt

CENTER FOR PHYSICAL SCIENCES AND TECHNOLOGY

Introduction

Hybrid perovskite materials have witnessed immense development in a range of optoelectronic devices, such as bright tunable LEDs, fast and sensitive photodetectors, and especially efficient solar cells. Chemical doping of perovskites with foreign atoms is a promising way to tailor material properties towards improving performance and stability of solar cells.

In this work [1], we discuss the efficiency increase in perovskite solar cells based on $MAPbI_3$ active layer, doped with 0.1 to 5 % of Sr^{2+} agent. A small amount <1 % of Sr^{2+} added to the perovskite improves open-circuit voltage by ~100 mV and consequently enhances the power conversion efficiency from 16.8 % to 17.8 %.

By employing transient photoluminescence, transient photocurrent and time-delayed collection field measurements we show that doping of $MAPbI_3$ by low content of Sr^{2+} additives (≤ 0.4 %) reduces the electron trapping efficiency. Whereas the reduced trapped electron density suppress nonradiative Shockley-Read-Hall recombination, which positively impacts open circuit voltage of perovskite solar cells.

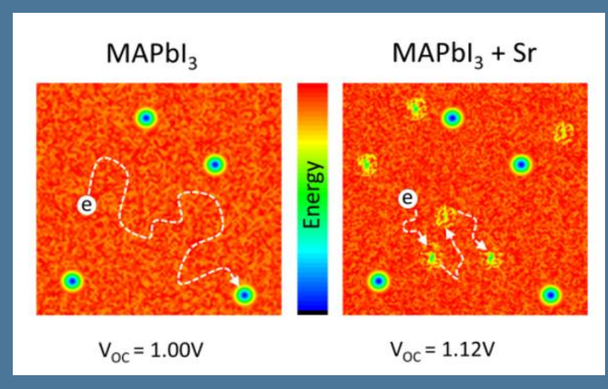

Fig. 1 Energy surface in $MAPbI_3$ film with and without small amount of Sr^{2+} doping

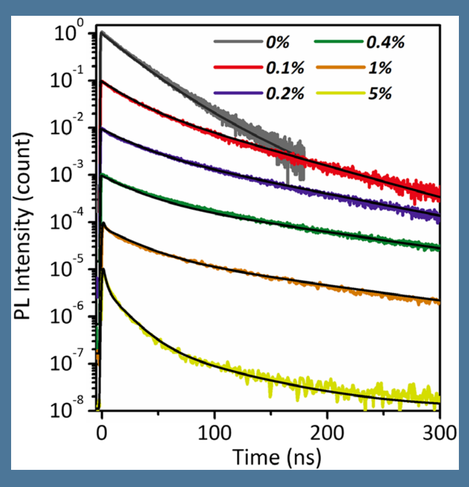

I. Transient Photoluminescence

Figure 2 shows the transient PL dynamics of the investigated $MAPbI_3$ films. The decay kinetics were fitted with multiexponential decay functions, and the relaxation times obtained from the approximations are provided in **Table 1.**

Sr^{2+} content in $MAPbI_3$	A1	τ1 [ns]	A2	τ2 [ns]	A3	τ3 [ns]
0%	0.84	20.2	0.22	37.6	-	-
0.1%	0.67	20.9	0.36	64.2	-	-
0.2%	0.65	26.9	0.35	93.5	-	-
0.4%	0.7	27.8	0.31	125.6	-	-
1.0%	0.59	1.4	0.55	27.8	0.20	128.9
5.0%	1.00	2.32	0.35	15.4	0.03	63.8

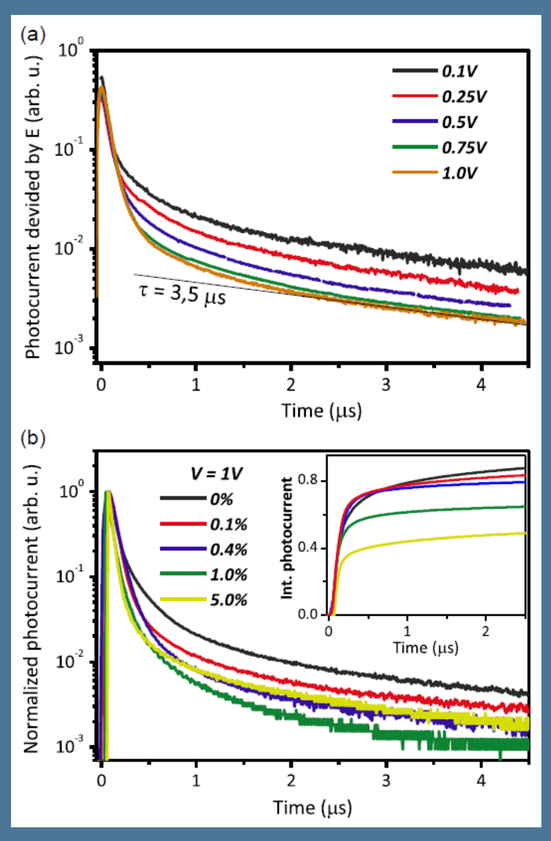

II. Transient Photocurrent

Figure 3 a) Photocurrent kinetics of pristine $MAPbI_3$ at indicated applied voltages and b) normalized photocurrent kinetics in samples with different Sr^{2+} concentrations at 1.0 V applied voltage. The insert in (b) shows integrated photocurrent kinetics (not normalized).

III. Time Delayed Collection Field

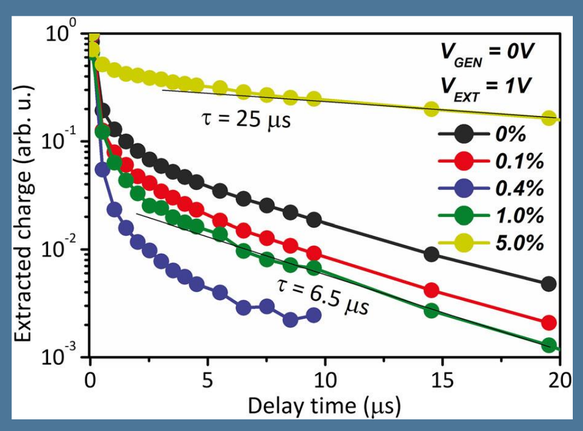

Figure 4. Dependencies of extracted charge value on delay time between the optical excitation pulse and electrical extraction pulse, obtained in different samples with 0 V generation and 1 V extraction voltages. The extracted charge was normalized to the extracted charge at zero delay time.

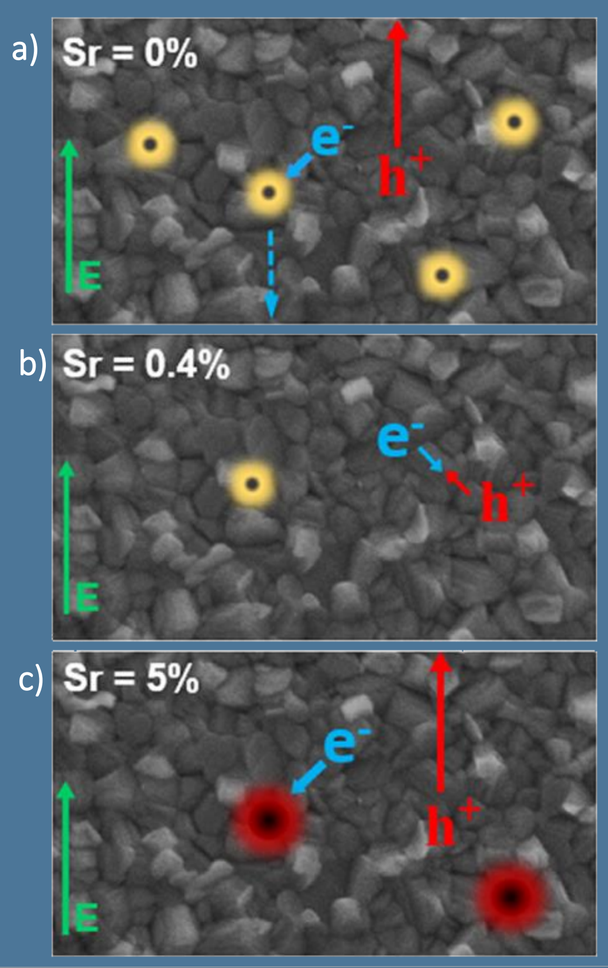

IV. CONCLUSIONS

Figure 5 summarizes results in a simple representative model (note that the SEM image does not correspond to the actual Sr^{2+} concentration sample but is used as a base for the schematic). Here, the green arrow shows the direction of an electric field.

In Figure 5a, the carrier dynamic is shown in a neat $MAPbI_3$ film. After the generation of charge carriers, holes are easily extracted (red arrow), whereas electrons swiftly fall (solid blue arrow) into a trap state (glowing yellow circle), from which they are slowly extracted by the electric field (dotted blue line).

The trap density decreases significantly in the presence of a low amount of Sr^{2+} additives (Figure 5b), which, despite resulting in increased V_{OC}, also enhances bimolecular recombination, as shown in the figure.

Higher Sr^{2+} concentration (Figure 5c), leads to the formation of deep trap states (glowing red circles). Electrons generated in the vicinity of such trap states fall into them and contribute to the slow photocurrent component.

References:

[1] Jasiūnas, R.; Gegevičius, R.; Franckevičius, M.; Phung, N.; Abate, A.; Gulbinas, V. Suppression of Electron Trapping in MAPbI3 Perovskite by Sr2þ Doping. Phys. Status Solidi RRL 2020, 5.

P2-5

Activity measurements of GMC superfamily flavoenzymes using Amplex Red assay

Rugilė Lukaševičiūtė[1] and Renata Karpicz[1]

[1]Department of Molecular Compound Physics, Center for Physical Sciences and Technology, Lithuania
rugile.lukaseviciute@ftmc.lt

Usage of biosensing systems containing enzymes is the promising and accurate method for detection of various compounds concentration in biological samples. Some of the most important properties describing enzyme are selectivity and enzymatic activity. In order to create and improve biosensor it is necessary to understand the properties of immobilized enzyme related to the influence of the surrounding environment.

The glucose-methanol-choline (GMC) superfamily is large family of oxidoreductases typically containing FAD-binding domain. Some members include oxidases like glucose oxidase (GOx), pyranose oxidase (POx), cholesterol oxidase (ChOx) and alcohol oxidase (AlOx). Electron donor substrates for GMC oxidoreductases range from various sugars and alcohols to cholesterol [1]. Amplex Red (10-acetyl-3,7-dihydroxyphenoxamine) is colorless and nonfluorescent reagent that is widely used as a probe to detect H_2O_2 in various biological samples [2]. In reactions catalysed by GOx, POx, ChOx and AlOx hydrogen peroxide is formed which then reacts with Amplex Red in the presence of horseradish peroxidase (HRP) and forms colored, highly fluorescent compound resorufin. Resorufin has exitation and emission maximum of 571 nm and because of high exitation coefficient enzyme activity can be determined fluorometrically or spectrophotometrically.

The purpose of this research was to evaluate activity of GOx, POx, ChOx and AlOx enzymes in different acidic values using Amplex Red reagent and determine optimal pH values for every enzyme. Our results show that Amplex Red assay can be used in measuring H_2O_2 released after enzymatic reaction. With decreasing acidity of the medium enzyme's activity increases. The amount of formed resorufin during enzymatic reactions increases respectively by reducing pH. At optimal medium acidity formed resorufin amount is largest whitch shows that enzyme's activity there is the highest.

REFERENCES

[1] L. Sutzl, G. Floey, E. J. Gillam, M. Boden, D. Haltrich „The GMC superfamily of oxidoreductases revised: analysis and evaluation of fungal GMC oxidoreductases," Biotechnology for Biofuels, 12, article 118, 2019.
[2] Baozhong Zhao, Fiona A. Summers, Ronald P. Mason „Photooxidation of Amplex red to resorufin: Implications of exposing the Amplex red assay to light," Free Radical Biology and Medicine, 53 1080-1087, 2012.

P2-6

Structural defect behavior of thermally annealed graphene, directly synthesized on Si(100) substrate using MW-PECVD

Šarūnas Jankauskas[1], Rimantas Gudaitis[1], Andrius Vasiliauskas[1] and Šarūnas Meškinis[1]

[1] *Institute of Materials Science of Kaunas University of Technology, K. Baršausko Str. 59, LT-51423, Kaunas, Lithuania*
Email: sarunas.jankauskas@ktu.lt

Graphene, material with exceptional physical properties, when synthesized using exfoliation, lacks certain qualities when grown directly on semiconducting surfaces. Although, microwave plasma enhanced chemical vapor deposition (MW-PECVD) can increase production rates of graphene, this form of synthesis introduces fair amount of defects [1]. To tackle this issue thermal annealing is rather straight forward method, which usually increases the overall quality of graphene by reducing the number of defects and other structural deformations, however there are other predominant effects, such as doping and strain, which could damage the sample [2]. Graphitic structure examination is usually based on Raman spectroscopy measurements which helps to determine both structure quality and thickness (graphene case).

In this work, four graphene samples were grown on Si(100) substrates, using MW-PECVD system (IPLAS Innovative Plasma Systems GmbH). Samples were thermally annealed using different temperatures (200-800°C) and environments (Ar, N2, vacuum) in order to thoroughly evaluate the changes of graphitic structures. All annealing's were performed for 30 min. The characterization of graphene samples was carried out using Raman spectrometer (Renishaw inVia, 532 nm, 4.5 mW) by analyzing changes in D, 2D and G bands. After annealing in Ar environment at temperatures, lower than 800°C, I_{2D}/I_G ratio changed from 1.04 to 0.47 and I_D/I_G ratio changed from 1.3 to 1.45, suggesting appearance of additional deformations. At higher temperatures (800°C, Ar) the graphitic structure collapses due to difference in thermal expansion coefficients between the graphene sheets and the substrate. Annealing in N_2 environment, I_{2D}/I_G changed from 1.6 to 0.62 and I_D/I_G from 1.56 to 2.02 hinting a huge increase in defective sites and strain development. After investigating changes in Raman spectrum after annealing in vacuum we have found out that I_{2D}/I_G changed from 0.61 to 0.23 and I_D/I_G from 1.53 to 1.71, showing that the dominant effect is rather defect formation than reduction, however values indicate a large number of layers, which could lead to inconclusive estimations.

In conclusion, we can see that our graphene structures are imperfect, which is true for such materials synthesized using MW-PECVD, however we believe that defect reduction could be achieved when samples exhibit more prominent graphene characteristics.

REFERENCES

[1] S. Zheng et al.; *RSC Advances* ***7*** (2017) pp. 33185-33193.
[2] M. Alyobi et al.; *Crystals* ***7*** (2017) pp. 349.

In-situ probing of SAM and tBLM layer formation on nanostructured gold by ATR-SEIRAS

Vaidas Pudžaitis[1], Martynas Talaikis[2], Gediminas Niaura[1]

[1]Department of Organic chemistry, Center for Physical Sciences and Technology, Sauletekio ave. 3, LT-10257 Vilnius, Lithuania.
[2]Institute of Biochemistry, Life Sciences Center, Vilnius University, Saulėtekio av. 7, LT-10257 Vilnius, Lithuania

INTRODUCTION

Attenuated total reflection surface-enhanced infrared reflection absorption spectroscopy (ATR-SEIRAS) is a powerful tool for in-situ analysis of molecular phenomena at the nanostructured metal surface. Various processes can be monitored in the water environment and under electrode potential control. Even more, a good signal-to-noise ratio provides the possibility to track the formation process of the self-assembled monolayers (SAMs). We demonstrate the use of ATR-SEIRAS for probing a two-step process of tethered bilayer lipid membrane (tBLM) formation. The tBLMs are living-cell membrane mimicking constructions which are used for biosensing applications, and as a platform for fundamental studies of biological membranes.

EXPERIMENT

During the first step (**Fig. 1A**), SAM layer is formed from lipid-like WC14 [20-tetradecyloxy-3,6,9,12,15,18,22-heptaoxahexatricontane-1-thiol] compound mix with β-mercaptoethanol (BME) on the nanostructured gold surface (Picture 1) [1]. Surface was prepared by electroless plating procedure on 0.25 µm polished silicon with 7.5 mM $NaAuCl_4$ solution containing Na_2SO_3, $Na_2S_2O_3$, NH_4Cl and NH_4F salts at room temperature [2].

Picture 1. AFM image of 0.25 µm polished Si prism surface (left) covered with gold by electroless plating (right).

SAM formation was monitored on FT-IR spectrometer equipped with MCT detector (Bruker, Vertex 80v) and VeeMax^{TM} ATR accessory (PIKE technologies) at 4 cm^{-1} resolution (~11 s/spectrum). EtOH solution on gold was used as a reference spectrum. Data representing 1mM WC14:BME (3:7 ratio respectively) SAM formation are shown in figure **1C**. By observing C-H stretching peaks of WC14 (**Fig. 1D**), it can be confirmed – initial SAM formation is complete in ~2-3 min time.

On a second step (**Fig. 1B**), ethanol was exchanged with water, which lead to WC14 methyl and ethyl peak shifts of 2 cm^{-1} towards lower energy (data not shown). This step was used as a reference for further FTIR observations. The tBLM was deposited from multilamellar vesicles (MVCs) prepared from 1,2-dioleoyl-sn-glycero-3-phosphocholine (DOPC) and cholesterol (CHOL) by pipetting 100 µl [3]. DOPC tBLM formation in ~15-20 min can be observed by plotting C-H stretch peak intensities against time (**Fig. 1F**). Additionally, water exchange from SAM's surface can be seen occurring concurrently (**Fig. 1E**).

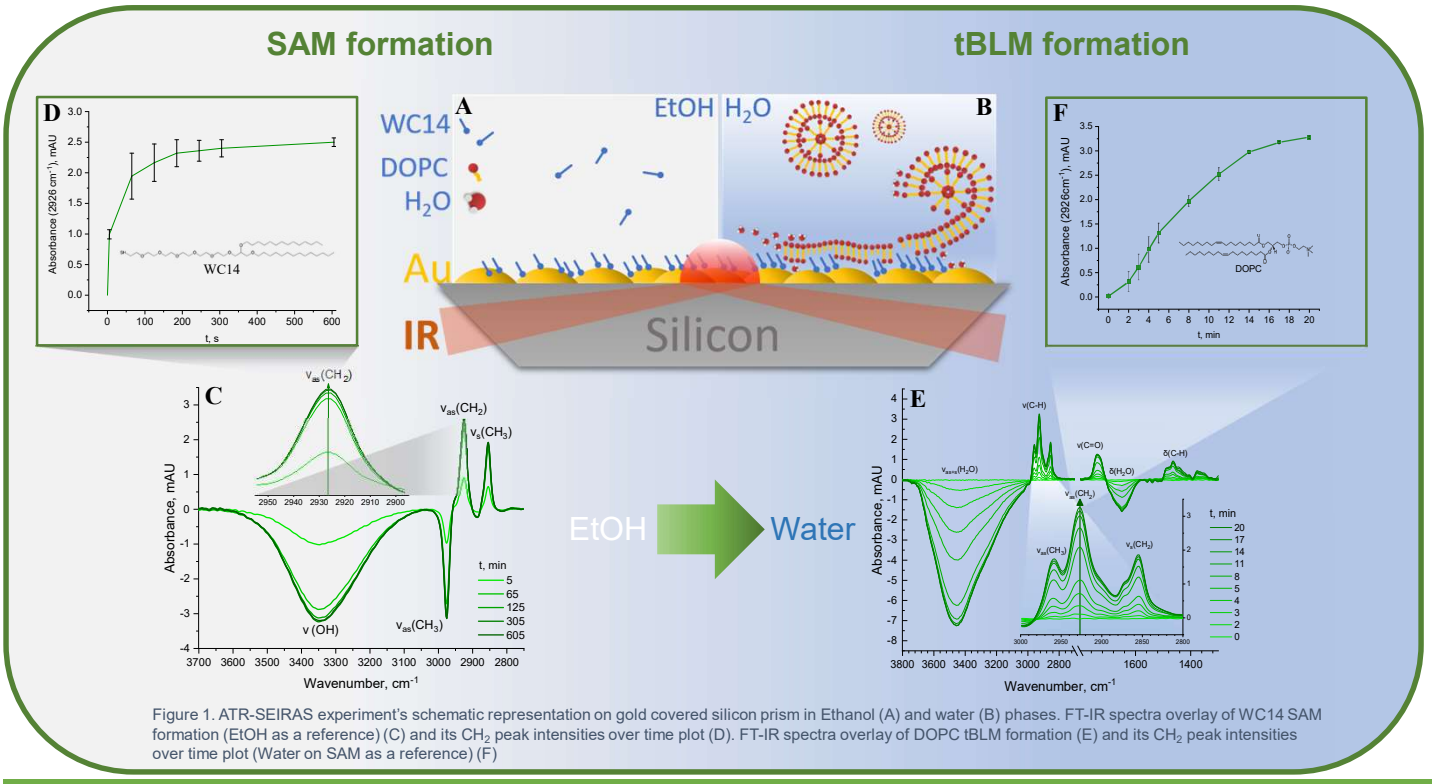

Figure 1. ATR-SEIRAS experiment's schematic representation on gold covered silicon prism in Ethanol (A) and water (B) phases. FT-IR spectra overlay of WC14 SAM formation (EtOH as a reference) (C) and its CH_2 peak intensities over time plot (D). FT-IR spectra overlay of DOPC tBLM formation (E) and its CH_2 peak intensities over time plot (Water on SAM as a reference) (F)

CONCLUSIONS

We demonstrate, that ATR-SEIRAS can provide complementary and in some cases unique molecular level information to already widely used methods. We show, that WC14 based SAM absorbs to the nanostructured gold surface in 2-3 min., while the DOPC based tBLM is formed in 20 min., pushing ethanol and water molecules (for SAM and tBLM respectively) away from the surface at a similar rate. Additionally, we see phase exchange (EtOH to H_2O) effect on C-H stretch vibrations, that confirms tighter SAM ordering.

REFERENCES

[1] R. Butvidyte et all; Langmuir 29 (2013) pp. 8645−8656.

[2] H. Miyake, S. Ye, M. Osawa; Electrochemistry Communications 4 (2002) pp. 973–977

[3] T. Ragaliauskas, M. Mickevicius, B. Rakovska, T. Penkauskas, D. J. Vanderah, F. Heinrich, G. Valincius; Biochimica et Biophysica Acta 1859 (2017) pp. 669–678.

P3-1

Impact of thin low specific conductivity layer on Fano resonance amplitude in an array of split ring resonators

A. Kamarauskas, G. Šlekas, D. Seliuta, and Ž. Kancleris

[1]*Center for Physical Sciences and Technology, Vilnius, Lithuania.*
Email: andrius.kamarauskas@ftmc.lt

The electromagnetic manifestation of Fano resonance was discovered in metasurface (MS) by Fedotov et al. [1] and later was widely investigated by many other researchers. Usually, it occurs in MS made from asymmetric split-ring resonators, but it was also observed in mirror-symmetric MS made from usual split-rings [2]. In this case, Fano resonance arises due to the interaction of 3rd order plasmonic mode and lattice mode.

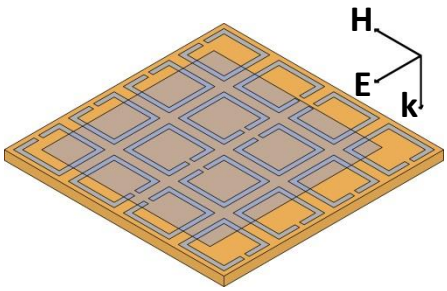

Fig. 1 The array of split-ring resonators with conductive layer on a top. The electric field is perpendicular to resonators' gap.

In this work, we investigate such a mirror-symmetric MS, the unit cell of which is shown in Fig. 1. The MS is made on 125 μm thickness substrate with a dielectric constant 2.2. The dimensions of the unit cell in the lateral plane are 1200 μm and 600 μm. The width of the resonators is 500 μm, the width of the strip and the gap is 50 μm. The resonators are made from 9 μm thickness cooper foil. The 2 μm thick layer with the same dielectric constant, which can be made from conductive polymer, is placed on the front or the back side of the substrate. Numerical modelling was performed using CST Microwave Studio software.

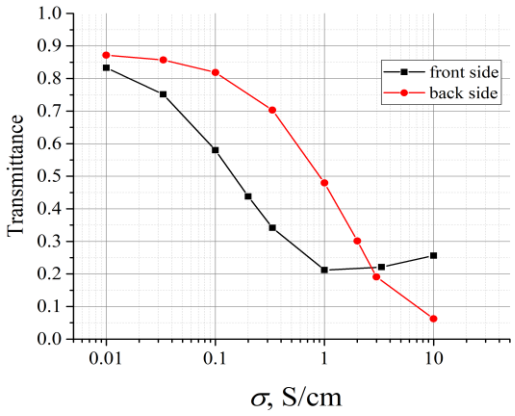

Fig. 2 The transmittance at the maximum amplitude of the Fano resonance versus specific conductivity of the layer. Resonance frequency at front side configuration is 222.9 GHz, at back side - 224.4 GHz.

Calculated dependences of transmittance at the maximum amplitude of the Fano resonance on specific conductivity of the layer situated on the front and back sides of the MS are shown in Fig. 2. It is seen that the difference in the transmitted signal through the MS is observed depending on the layer position when the conductivity of the layer is as low as 0.01 S/cm. On the one hand, the decrease of the transmittance on the conductivity is larger when the layer is placed on the resonator plane. On the other hand, the dynamic range is wider in the back side configuration. High sensitivity of the Fano resonance amplitude in the proposed structure to the low-to-mid conductivity planar sheet could be useful in sensing applications or modulation of electromagnetic waves.

REFERENCES

[1] V. Fedotov et al., *Phys. Rev. Lett.* **99**, (2007) 147401.
[2] D. Seliuta et al., *Optics Letters* **44**, (2019) pp. 759-762.

Black silicon based substrates for surface enhanced Raman spectroscopy

Ieva Matulaitienė[1], Lena Golubewa[1], Renata Karpicz[1], Algirdas Selskis[1] and Polina Kuzhir[2,3]

[1] Center for Physical Sciences and Technology, Sauletekio Ave. 3, LT-10257 Vilnius, Lithuania.
[2] Institute for Nuclear Problems of BSU, Bobruiskaya 11, 220030 Minsk, Belarus.
[3] Institute of Photonics, University of Eastern Finland, Yliopistokatu 2, FI-80100 Joensuu, Finland.
Email: ieva.matulaitiene@ftmc.lt.

The evolution of new technologies brought to humankind not only comfortable environment, but also new treats. The major treat is environmental pollution that leads to various diseases and requires new processes, diagnostic systems. Surface enhanced Raman spectroscopy (SERS) is one of the most sensitive techniques of vibrational spectroscopy that gives information about the material in molecular level. Nowadays there are plenty techniques for SERS substrates fabrication, that must meet three conditions: certain metal surface (Au, Ag, Cu), the surface is rough and sample must be near or adsorbed at the surface [1]. In this study, we represent black silicon based substrates (bSi) for SERS application.

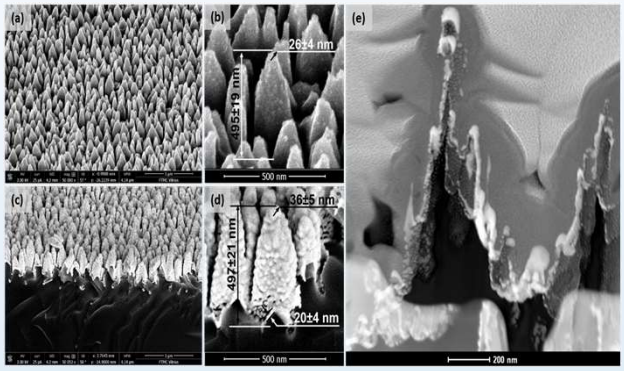

Fig.1. SEM images of bSi (a, b) and bSi/Au (c, d) substrates; (e) TEM image of the silicon cone covered by 25-50 nm thick gold layer.

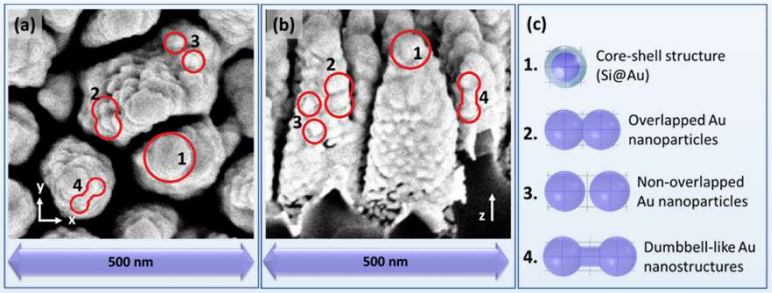

Fig. 3. (a) top-view SEM image of bSi/Au showing horizontally (perpendicular to the wavevector k $^{\rightarrow}$) oriented bi-spheres and dumbbell-like particles; (b) side-view SEM image of bSi/Au showing vertically (along the wavevector k $^{\rightarrow}$) oriented bi-spheres and dumbbell-like particles; (c) elementary nanostructures selected for numerical simulation of the E-field enhancement.

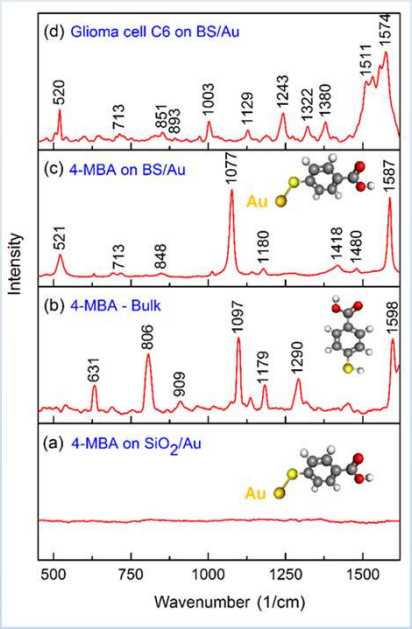

Fig. 2. Raman spectra of 4-MBA monolayer on SiO_2/Au smooth substrate (a), of bulk 4-MBA (b), and SERS spectra of 4-MBA (c) and living rat glioma cell (d) on the bSi/Au substrate. Excitation wavelength is 785 nm.

The enhancement factor of the SERS-active bSi/Au substrate $\approx 2 \times 10^8$.

$$EF = \frac{I_{BSi/Au} / N_{BSi/Au}}{I_{bulk} / N_{bulk}}$$

where $I_{BSi/Au}$ ($N_{BSi/Au}$) and I_{bulk} (N_{bulk}) are Raman intensities (numbers of irradiated molecules) of 4-MBA monolayer on the bSi/Au substrate and bulk 4-MBA on the SiO_2 substrate obtained at the same laser power and time accumulation, respectively.

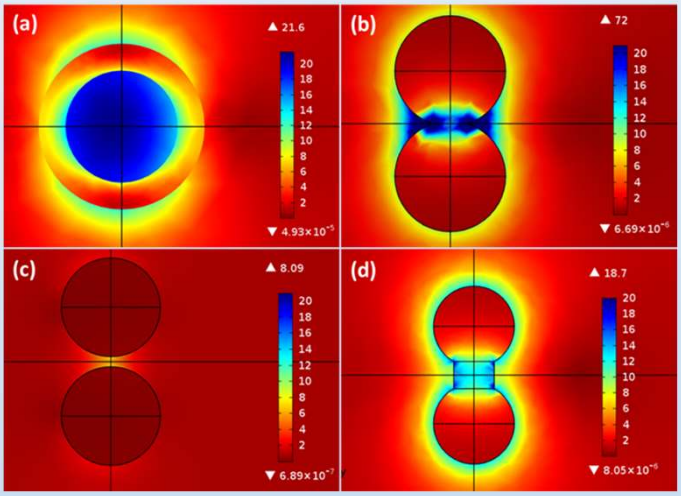

Fig. 4. E-filed enhancement maps at the irradiation wavelength of 790. (a) Si@Au (44nm@21nm), (b) Au bi-sphere (r = 25 nm, distance 47.5nm), (c) Au bi-sphere (r = 25 nm, distance 55 nm), (d) dumbbell-like structure (r_0 = 13.5 nm). Δ and ∇ are maximum and minimum values of the E-filed enhancement, respectively.

Assignments of vibrational bands of 4-MBA in solid and adsorbed

Raman solid state (cm^{-1})	bSi/Au/ 4-MBA (cm^{-1})	Calculated Au_1- 4-MBA (cm^{-1})	Peak assignment
–	521	498	ν(CS)
631	631	642	ν_{6b}
–	693	–	γ(CH) out-of-plane
–	713	–	ν_{4b} + γ(CCC) out-of-plane
806	–	766	ν_{10a}
–	848	–	β(COO^-)
909	–	–	β(SH)
–	1013	–	in-plane ring breathing, b_2
1097	1077	1059	ν_{12} (a_1) in-plane aromatic ring breathing mode + ν(CS), a_1
–	1142	–	ν_{15} (b_2) δ(CH) deformation
1179	1180	1162	ν_9 (a_1) δ(CH) deformation
1290	–	–	ν_3
–	–	1326	ν (COO^-) stretching mode
–	1418	–	ν (COO^-) stretching mode
–	1480	–	ν(CC) + γ(CH)
1598	1587	1585	ν_{8a} (a_1) totally symmetric aromatic ring vibration

We perform a new bSi material possessing the unique properties allowing the use of the bSi sputtered with gold substrate as a highly sensitive stable SERS-active platform for detection of not only trace amounts of small organic molecules, but also living cells. The produced bSi surface due to its significant roughness, submicron regular cone structures evenly distributed over the entire surface, their high density allows to obtain the SERS-active surface with sufficiently good EF of about 108 and to create evenly distributed hot spots through the deposition of only 25÷50 nm gold layer instead of 100-400 nm traditionally used, significantly reducing production costs. Simulation results fully proved high E-field enhancement and revealed the major impact of LSPR in SERS properties of BS/Au substrates. Moreover, it was established that only vertical nanostructures alignment along bSi/Au cones provides appearance of the resonant absorption in NIR and significant E-field enhancement with EF of 10^4-10^8.

The BS/Au substrates may be easily fabricated in a large-scale using existing techniques, with the tune control of specific surface parameters, providing efficient enhancement, stability and reproducibility, and is a promising substrate for biosensor systems.

Acknowledgements This work was financially supported by joint project no. S-LB-19-4 from the Research Council of Lithuania Foundation, the Belarusian Republican Foundation for Fundamental Research (BRFFR) project F19LITG-003.

Terahertz detection and noise properties of $(Cd_{1-x}Zn_x)_3As_2$

I. Yahnyuk[1], D. But[1], D. Yavorskiy[1], G. Grabecki[2], K. Grasza[2], W. Knap[1,3] and S. Rumyantsev[1]

[1] International Research Centre CENTERA, Institute of High Pressure Physics, Polish Academy of Sciences, 01-142 Warsaw, Poland
[2] Institute of Physics PAS, al. Lotników 32/46, PL 02-668 Warsaw, Poland
[3] Laboratoire Charles Coulomb (L2C), UMR CNRS 5221, F-34095 Montpellier, France

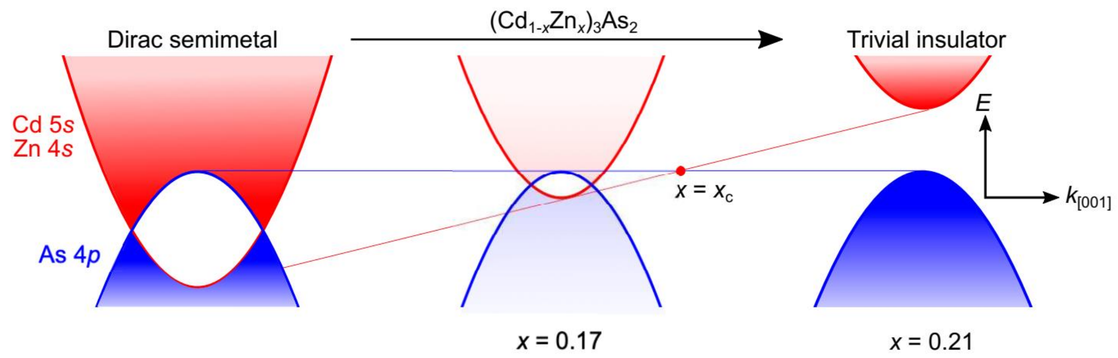

Evolution of the surface transport through topological phase transition. Zn doping-induced topological phase transition from a Dirac semimetal (DSM) to a trivial insulator in $(Cd_{1-x}Zn_x)_3As_2$ [1]

Dirac semimetals

- Dirac dispersion in the touch points
- Valence and conduction band touching in discrete points
- Robust against perturbations

Although Cd_3As_2 as a semiconductor material is known for almost a century, it has not found wide applications so far. The main reasons are difficulties in technology and doping. However, the large tunability of band gap from 0 eV for Cd_3As_2 to 1 eV for Zn_3As_2 makes it an ideal material for infrared and terahertz applications. Also interests in this material was renewed by the theoretical study showing the presence of a pair of symmetry protected three-dimensional Dirac cones [2]. Indirect proof of this theoretical prediction is the extremely high electron mobility and the strong dependence of the electrons effective mass on their concentration. Extraordinary electronic properties and high mobility make it interesting for terahertz applications.

In this work, crystals of $(Cd_{0.4}Zn_{0.6})_3As_2$ were grown by were grown by horizontal Bridgman method [3]. The studied samples of bulk material were in a few millimeters in size with Hall bar geometry and indium contacts.

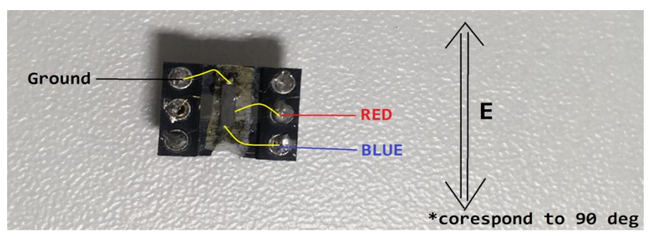

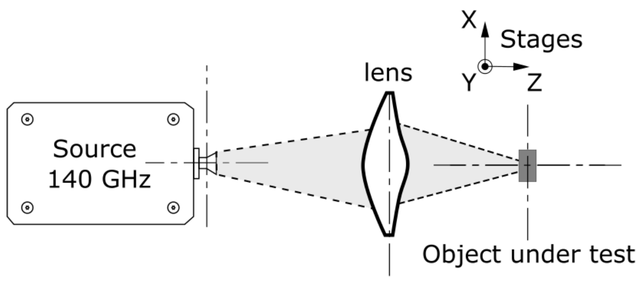

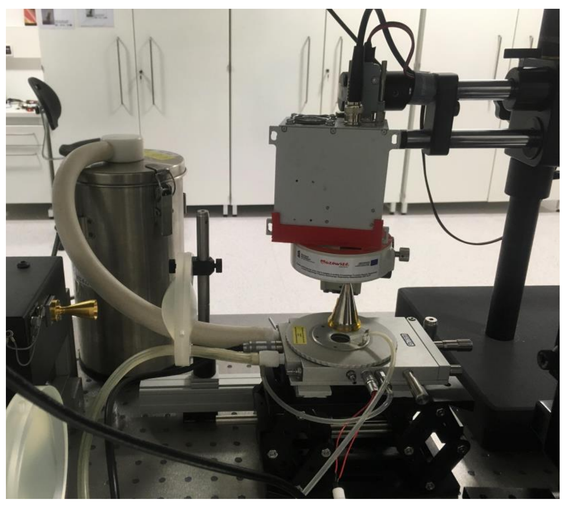

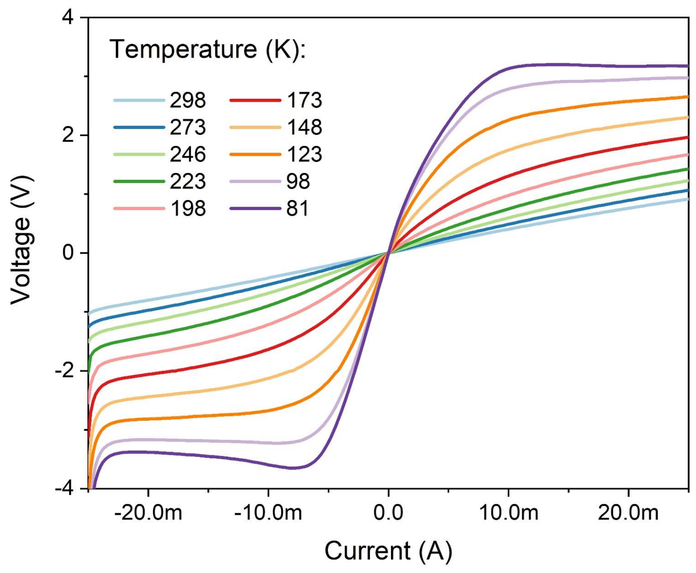

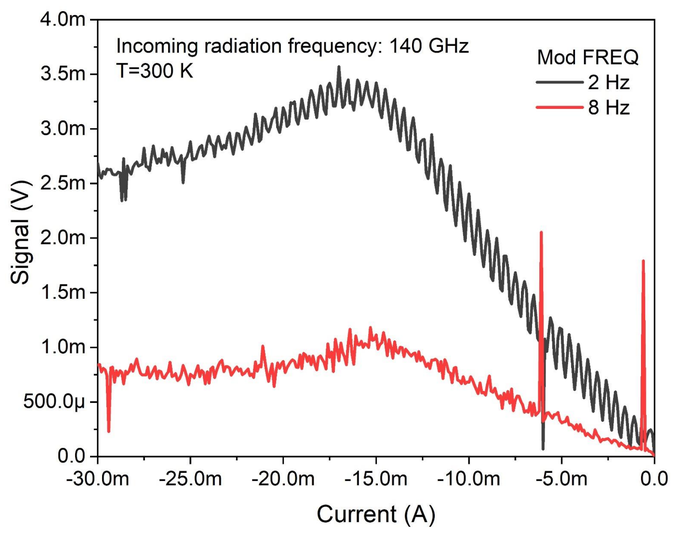

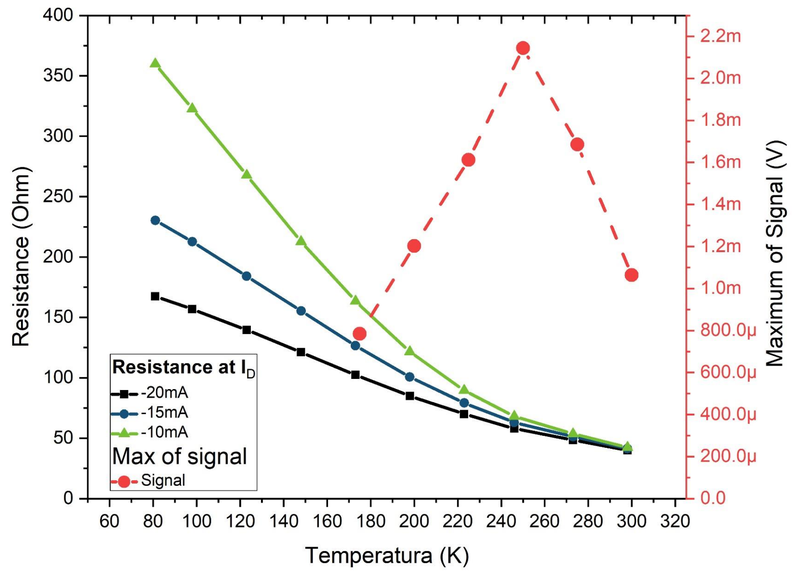

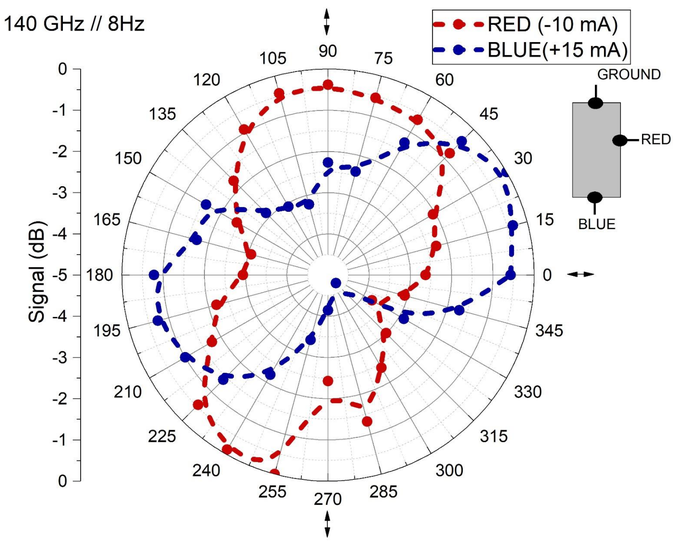

Conclusions

- ❑ The high frequency detection was studied at sub-terahertz frequencies of 100GHz and 140 GHz.
- ❑ Relatively high amplitude of the response in a few millivolt ranges for an incident power of approximately 35 mW.
- ❑ The current dependence of the response had some signs of the bolometric mechanism.

Reference:

[1] Shinichi Nishihaya, et.al, [Nat.Comm. 10, 2564 (2019)]
[2] Z. Wang, H. Weng, Q. Wu, X. Dai, and Z. Fang, Phys. Rev. B 2013, 88, 125427.
[3] G. Grabecki et al., Apparent metal-insulator transition in $(Cd_{0.4}Zn_{0.6})_3As_2$ (in preparation)

Acknowledgements: The „Center for Terahertz Research and Applications (CENTERA)" project is carried out within the 'International Research Agendas' programme of the Foundation for Polish Science co-financed by the European Union under the European Regional Development Fund.

European Funds Smart Growth | Republic of Poland | FNP Foundation for Polish Science | European Union European Regional Development Fund

CENTERA (MAB/2018/9) Institute of High Pressure Physics PAS, Sokołowska 29/37 Str, PL-01-142 Warsaw

P3-4

Enhanced sensitivity AlGaN/GaN HEMT terahertz detector without ungated regions

Juozas Vyšniauskas[1], Kęstutis Ikamas[1,2] and Alvydas Lisauskas[1,3]

[1] *Institute of Applied Electrodynamics and Telecommunications, Vilnius University, Vilnius, Lithuania.*
[2] *Department of Defence Technologies, Military Academy of Lithuania, Vilnius, Lithuania.*
[3] *CENTERA Labs, Institute of High Pressure Physics PAS, Warsaw, Poland.*
Email: juozas.vysniauskas@ff.vu.lt.

AlGaN/GaN HEMTs [1,2] and nMOS [3] transistors are reported as the most sensitive field effect transistor-based terahertz detectors. The advantage of HEMT is high electron mobility (up to 1500 cm^2/Vs) and the disadvantage is the presence of passive ungated regions which introduce additional series impedance contributing to the loss of high-frequency signal. The advantage of nMOS is the absence of ungated regions and the disadvantage is low electron mobility (about 250 cm^2/Vs) due to high acceptor density (about 2e18 cm^{-3}) in the channel.

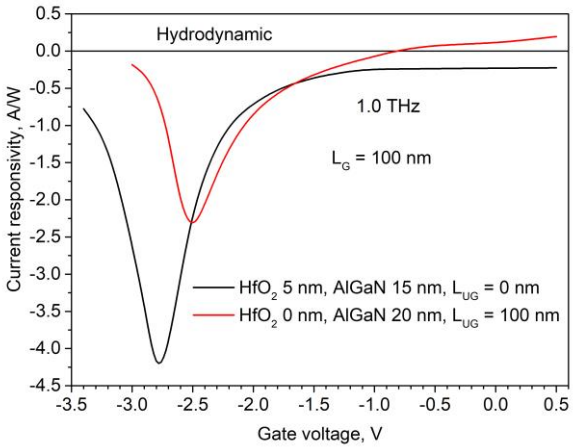

Fig. 1 Current responsivity of the HEMT without and with ungated regions L_{UG} and gate length L_G.

Here, we propose the HEMT-based THz detector with 5 nm HfO_2 dielectric between the gate electrode and the AlGaN layer, which allows to separate the gate from the source and drain terminals without involving ungated regions.

For numerical calculations of detector characteristics, we have employed two-dimensional hydrodynamic modeling performed with Synopsys TCAD Sentaurus program package comprising Poisson's equation, continuity equation, current density equation and energy balance equation for electrons and holes. It accounts for the formation of spontaneous and piezoelectric polarization charges in GaN and AlGaN layers, as well as the dependence of carrier mobility on doping density and carrier temperature.

The comparison of current responsivity of the HEMT with and without ungated regions and the gate length L_G = 100 nm is shown in Fig. 1. The results clearly indicate that the presence of ungated regions with the length L_{UG} = 100 nm reduces the maximum of the current responsivity at 1 THz by about 2 times. The minimum NEP at 1 THz is about 3 times lower in the HEMT without ungated regions.

REFERENCES

[1] M. Bauer at al; IEEE Transactions on Terahertz Science and Technology **9,** 430 (2019).
[2] J. Sun at al; Applied Physics Letters **116**, 161109 (2020).
[3] K. Ikamas at al; IEEE Electron Device Letters **39**, 1413 (2018).

Performance of Titanium-based Microbolometers for Monitoring of Spatial Beam Profile in Terahertz Time-Domain Systems

Liang Qi[1], Linas Minkevičius[1], Andrzej Urbanowicz[1], Andrej Švigelj[2], Janez Trontelj[2], Domas Jokubauskis[1] and Gintaras Valušis[1]

1 Center for Physical Sciences and Technology, Saulėtekio Ave. 3, LT-10257 Vilnius, Lithuania

2 Laboratory for Microelectronics, Faculty of Electrical Engineering, University of Ljubljana, Tržaška 25, 1000 Ljubljana, Slovenia

Email: liang.qi@ftmc.lt

Spatial mode profile and its control in terahertz (THz) imaging and spectroscopic systems is one of the most important constituents to enable high data quality. Moreover, convenience in use and abilities for precise optical alignment without additional optical components would be attractive advantage in practical implementation of the systems.

In this communication, convenient and easy-to-use both resonant and broadband antenna coupled ultrasensitive titanium-based microbolometers are demonstrated for fine adjustment and control spatial mode profiles in THz time-domain systems. The devices were found well-suited for implementation for medical imaging aims [1].

Three types of microbolometers [2] with the narrow band dipole antenna of 0.3 THz, 0.7 THz and a log-periodic broadband antenna [3] were explored. Femtosecond laser with a wavelength of 780nm, pulse duration of 90 fs and output power of 150mW at 80 MHz pulse repetition rate was used for optical excitation. The photoconductive antennas made from LT-GaAs offers a wide transmission spectrum from 0 to 5THz in the experiment.

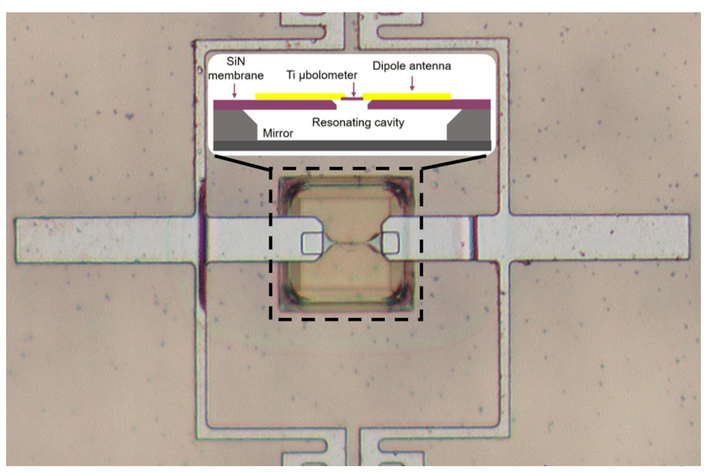

Fig. 1. The scheme of THz titanium-based microbolometer with dipole antenna.

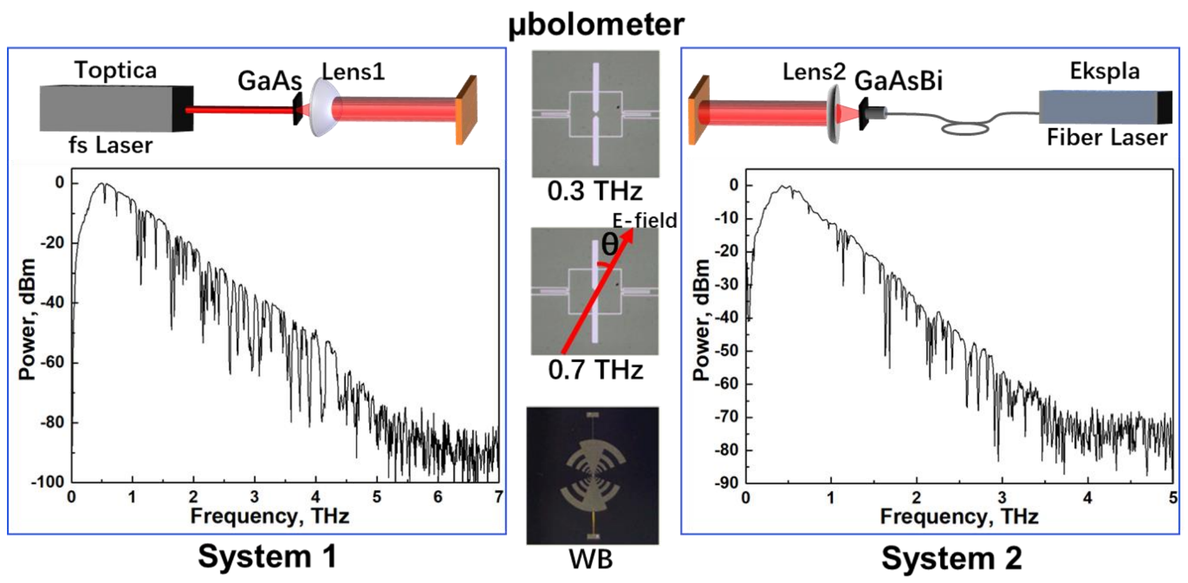

Fig. 2. The schematic diagrams and parameters of TDS setups in **System 1** and **System 2**, photos of three microbolometers. The angle θ is defined on the photo of 0.7THz detector.

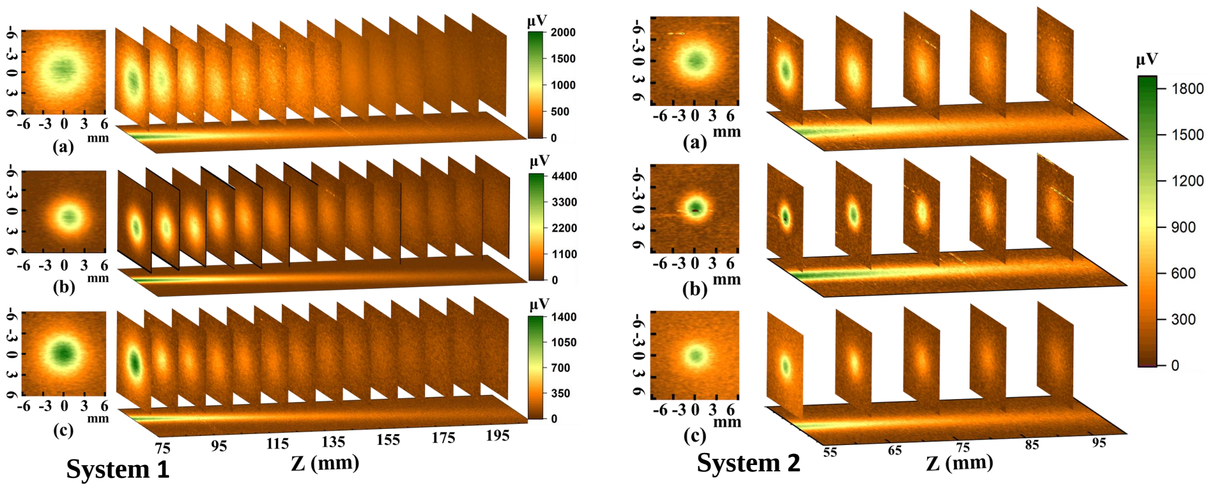

Fig. 3. The beam profile evolution of System 1 and System 2, separately recovered by three different detectors. (a) recorded by 0.3THz detector, (b) recorded by 0.7THz detector, (c) recorded by broadband detector.

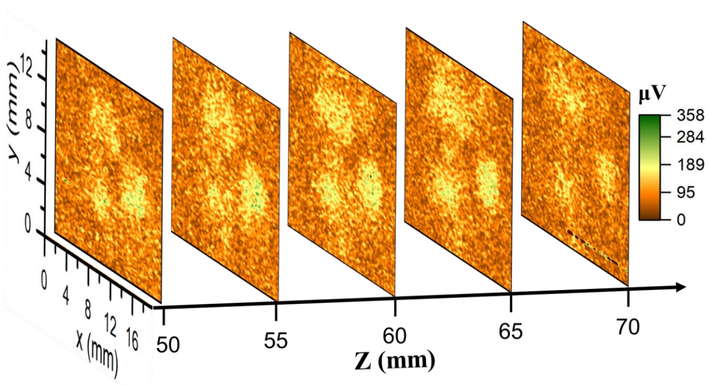

Fig. 5. The spatial characteristic of System 1 without Lens1 along z- axis detected by 0.7 THz microbolometer.

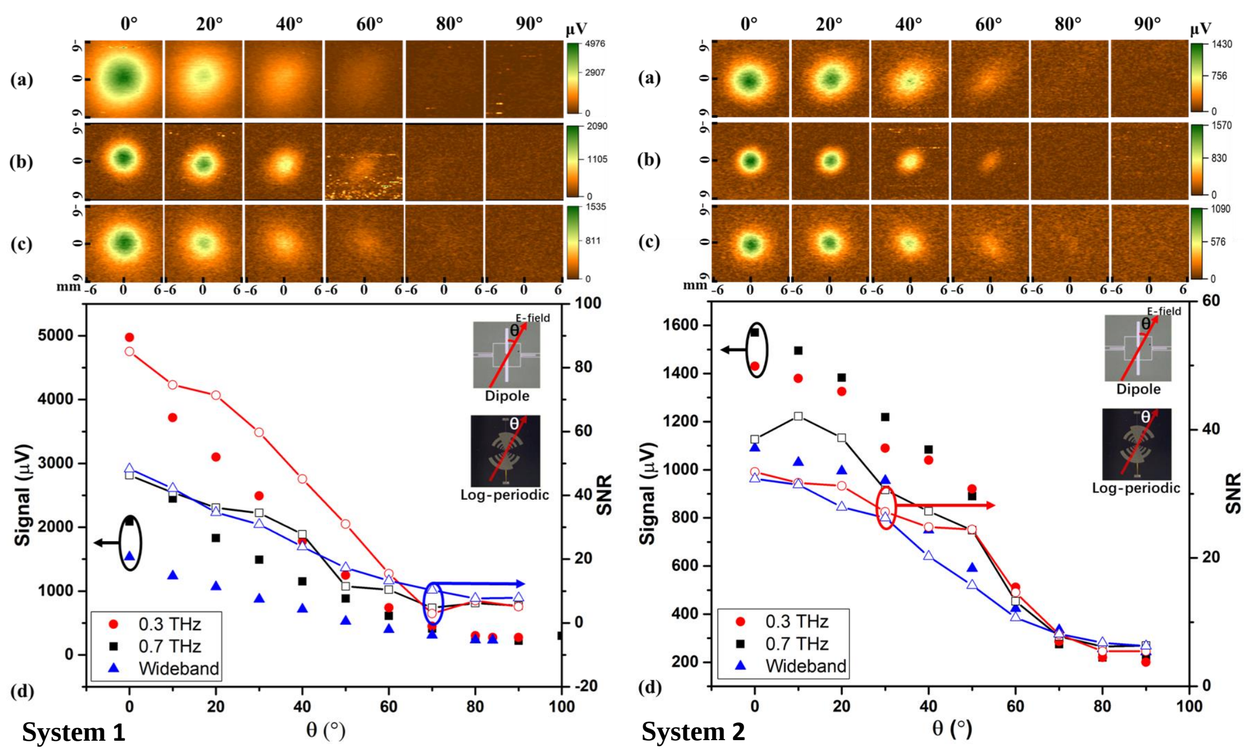

Fig. 4. The evolution of beam profile, peak power and SNR with different polarization in System 1 and System 2.

CONCLUSIONS

Spatial mode profiles and polarization-resolved mode structures are recorded by titanium-based microbolometers in two THz time-domain systems. It is found that three microbolometers reproduce well the spatial mode profile of time-domain spectrometer. Polarization-sensitive mode control possibilities are also examined in details.

REFERENCES

[1] I. Kašalynas, R. Venckevičius, L. Minkevičius, A. Sešek, F. Wahaia, V. Tamošiūnas, B. Voisiat, D. Seliuta, G. Valušis, A. Švigelj, and J. Trontelj, Sensors 16, (2016) 432.

[2] J. Trontelj, G. Valušis, R. Venckevičius, I. Kašalynas, A. Sešek and A. Švigelj; Terahertz Emit. Receiv. Appl. V 9199(2014) pp. 91990K.

[3] L. Minkevičius, L. Qi, A. Siemion, D. Jokubauskis, A. Sešek, A. Švigelj, J. Trontelj, D. Seliuta, I. Kašalynas and G. Valušis; Appl. Sci.10(2020) pp.3400.

Laser system for pumping THz and coherent X-ray sources of secondary radiation

Paulius Mackonis, Augustinas Petrulėnas, Vytenis Girdauskas and Aleksej Rodin

Solid State Laser Laboratory, Center for Physical Sciences and Technology, Savanoriu 231, LT-02300 Vilnius, Lithuania.

We demonstrate compact TW-class VIS-NIR wavelength range Noncollinear Optical Parametrical Chirped Pulse Amplifier (NOPCPA) with an almost lossless spectral bandwidth due to the formation of “M”-shaped picosecond pumping pulses after the SHG-conversion. Moreover, the reuse of depleted pulses after the first SHG cascade increases the overall efficiency.

Compact TW-class VIS – NIR wavelength range laser system

The progress of natural science as well as a paradigm shift in the economy became inconceivable without the implementation of superstrong electromagnetic fields. However, the commissioning of high-intensity lasers within ELI framework is more a form of budget redistribution than a solution, because the cumbersome and time-consuming laser architecture is doomed to downtime, while scientists and technologists remain on the waiting list.

Ultrashort, high energy, tunable wavelength laser pulses are in demand for a wide range of applications in ultrafast and strong field physics. Of great interest is their use for driving secondary radiation sources, such as the generation of THz and attosecond X-ray pulses. In addition, filamentation of ultrahigh intensity laser pulses in air opens up unprecedented opportunities for remote gas sensing. Recent studies have shown that an increase in the wavelength of the driving laser radiation makes it possible to generate higher photon energy attosecond X-ray pulses [1], as well as improve the efficiency of THz generation [2]. Furthermore, filamentation in air also benefits from longer driving wavelength because the wavelength scaling of the critical power of self-focusing allows more energy to be contained in a single filament.

In this work we present a cost-effective laser system that provides a choice of output pulses: >20 mJ, 1.2 ps with M^2<1.1 at 1030 nm [3] or >2 mJ, <20 fs with M^2~1.2 at 790 nm [4], as well as probe supercontinuum (SC) at 500 – 2400 nm [5]. A multi-octave SC in the range up to 2400 nm allows the use of a similar OPCPA architecture to develop a sub-TW laser in the 2 μm spectral range for the high order harmonics generation or remote sensing of gases by filamentation. However, to eliminate the need for expensive periodically poled nonlinear crystals, we are developing an alternative concept for broadband Transient Stimulated Raman Chirped Pulse Amplification (TSRCPA) [6].

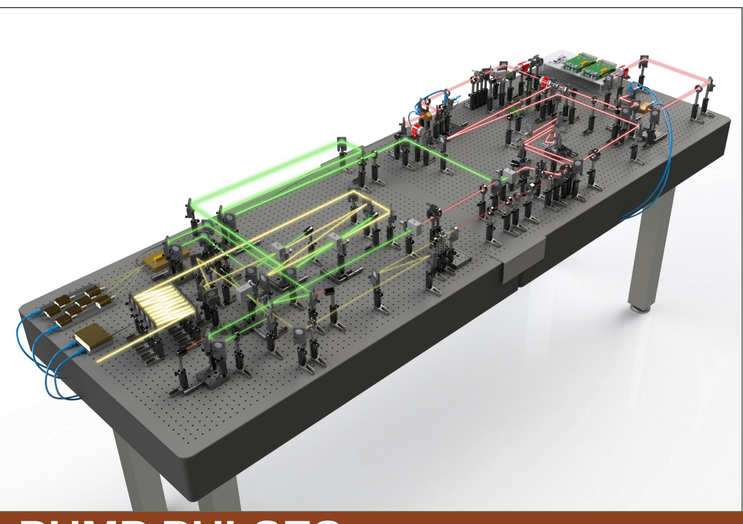

PUMPING SOURCE
Yb:YAG CPA and Pulse Compresssor

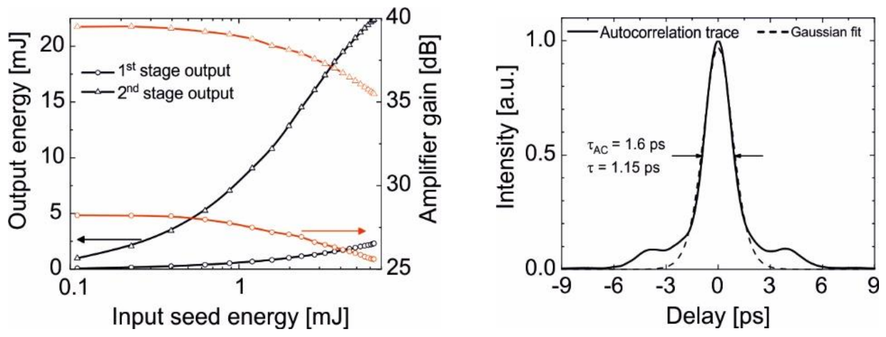

Fig. 1 The output energy (black) and gain (red) of CPA versus the seed energy (left) and autocorrelation trace of amplified pulses after compression (right).

- ✓ Amplified pulses with a total gain of ~3.500, an output energy of up to **22 mJ**.
- ✓ Pulses energy stability better than 1 %.
- ✓ Pulse compression up to **~1.2 ps**.
- ✓ Excellent beam quality M^2 **< 1.1.**

OPCPA SEED AND PUMP PULSES
Supercontinuum and Second Harmonic Generation

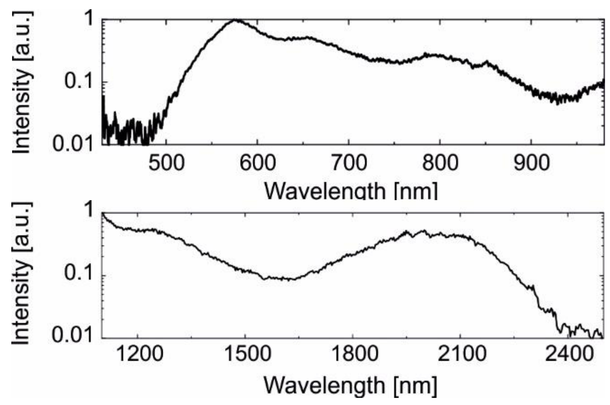

Fig. 2 Supercontinuum spectra in 15 mm YAG crystal.

- ✓ Stable single-filament supercontinnum spanning **~500 nm to ~2400 nm** in YAG rod of **15 mm** length.
- ✓ SC shows an energy stability exceeding the pumping laser.

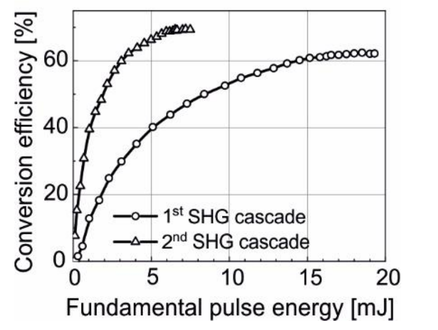

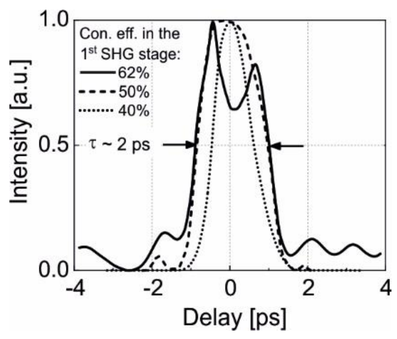

Fig. 3 SHG Conversion efficiency in the first and second SHG cascades (left). Temporal profiles of the second harmonic pulse after the second SHG cascade (right).

- ✓ Compressed pulses converted to the second harmonics in LBO and BBO crystals with **62%** and **70%** efficiency: overall ~**85%** efficiently.
- ✓ After the first SHG cascade: **12 mJ** output energy at 515nm and **~ 1.2 ps** pulsewidth.
- ✓ Further frequency doubling of depleted pulses in BBO provides “M”-shaped pump pulses at 515 nm with **5 mJ** output energy and **~2 ps** pulsewidth.

IN PROGRESS:
compact femtosecond VIS – NIR – SWIR laser system

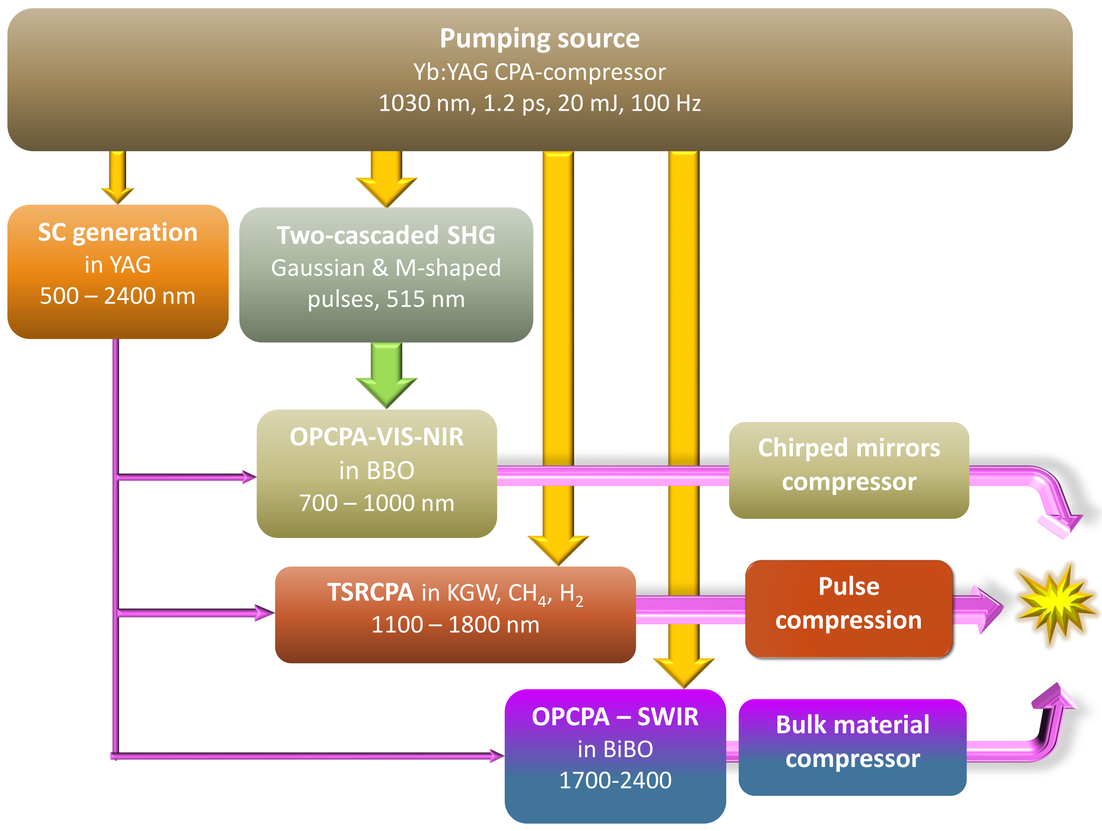

Fig. 4 Layout of a compact femtosecond VIS – NIR – SWIR laser system.

OPCPA – VIS-NIR

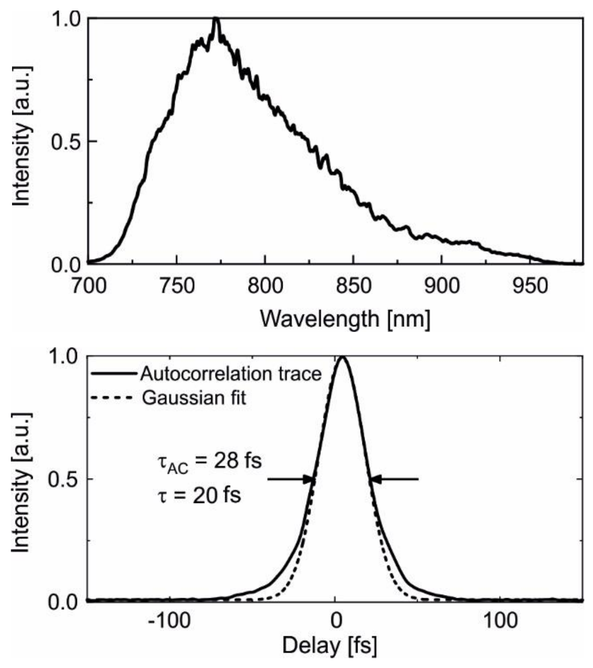

Fig. 5 Spectrum of amplified pulses after three OPCPA stage (top) and autocorrelation trace after comression (bottom).

- ✓ The pump-to-signal efficiency of **~20%** and the pulse energy of **~2.1 mJ** after the third OPCPA stage was reached.
- ✓ Amplified spectrum corresponding to Fourier-limited pulsewidth of **~8.6 fs**.
- ✓ Pulse compression up to **20 fs**.
- ✓ Beam quality M^2 **< 1.25.**

Transient Stimulated Raman Chirped Pulse Amplification

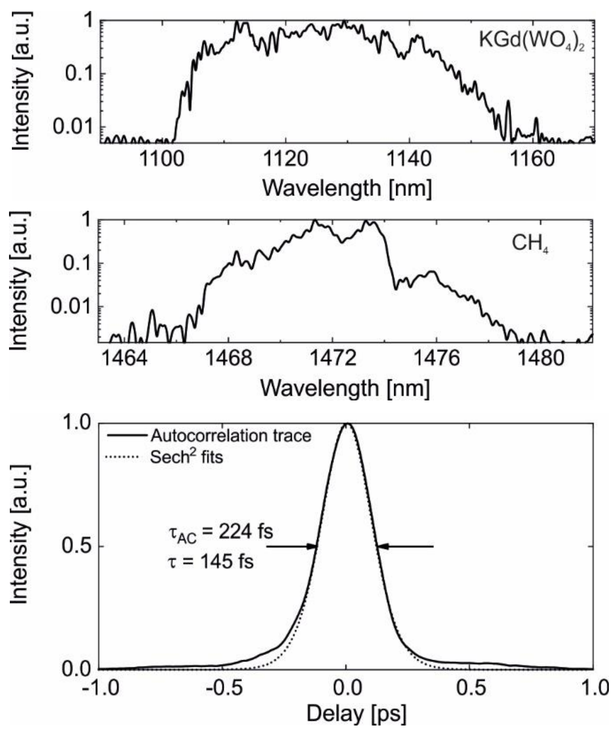

Fig. 6 TSRCPA output spectra in $KGd(WO_4)_2$ (top) and CH_4 (middle). Autocorrelation trace of compressed pulse after TSRCPA in $KGd(WO_4)_2$ crystal (bottom).

- ✓ Frequency shift during amplification of chirped SC pulses in a stimulated Raman amplifier based on solids or gases.
- ✓ Possible pulse compression.

Conclutions & future work

- Recycling of depleted pulses at fundamental wavelength after the first SHG stage improves the overall harmonics conversion efficiency up to 85%**.**
- The use of “M”-shaped pump pulses made it possible to maintain a wide spectral bandwidth of amplified pulses in OPCPA stages with a high gain, while Gaussian pump pulses provided efficient energy extraction at the last stage.
- Laser system was built with an output energy of 2.1 mJ at a repetition rate of 100 Hz with support of a spectral bandwidth corresponding to a transform-limited pulsewidth of 8.6 fs. Pulse compression up to 20 fs at 790 nm was demonstrated.
- Transient Stimulated Raman Chirped Pulse Amplification shows a potential as an alternative to OPCPA or a complimentary method for developing intense femtosecond laser pulse source with frequency conversion.

Acknowledgment

- Two of the co-authors are grateful to Eksma Ltd for providing student scholarships.
- This research was sponsored in part by the NATO SPS Programme under grant G5734.
- The solutions developed during the project were implemented at Ekspla Ltd in technological and scientific lasers.

References

[1] M.C.Chen, P.Arpin, T.Popmintchev, M.Gerrity, B.Zhang, M.Seaberg, D.Popmintchev, M.M.Murnane and H.C.Kapteyn, “Bright, Coherent, Ultrafast Soft X-Ray Harmonics Spanning the Water Window from a Tabletop Light Source,” Phys. Rev. Lett. 105, 173901 (2010).

[2] M.Clerici, M.Peccianti, B.E.Schmidt, L.Caspani, M.Shalaby, M.Giguere, A.Lotti, A.Couairon, F.Legare, T.Ozaki, D.Faccio and R.Morandotti, “Wavelength Scaling of Terahertz Generation by Gas Ionization,” Phys. Rev. Lett. 110, 253901 (2013).

[3] P.Mackonis, A.Rodin, “Laser with 1.2 ps, 20 mJ pulses at 100 Hz based on CPA with a low doping level Yb:YAG rods for seeding and pumping of OPCPA,” Opt. Express 28(2), 1261-1268 (2020).

[4] P.Mackonis, A.Rodin, “OPCPA investigation with control over the temporal shape of 1.2 ps pump pulses,” Opt. Express 28(8), 12020-12027 (2020).

[5] P.Mackonis, A.Petrulenas, V.Girdauskas, and A.M.Rodin, “Stable 1100 - 2400 nm supercontinuum in YAG with picosecond pumping for simplified OPCPA,” in 2019 Conference on Lasers and Electro-Optics Europe and European Quantum Electronics Conference, OSA Technical Digest (Optical Society of America, 2019), paper ca_p_43.

[6] P.Mackonis, A.Rodin, A.Petrulenas, V.Girdauskas and A.Michailovas, “Two-stage transient stimulated Raman chirped pulse amplification in $KGd(WO_4)_2$ with compression to 145 fs,” (to be published).

Laser system for pumping THz and coherent X-ray sources of secondary radiation

Paulius Mackonis, Augustinas Petrulenas, Vytenis Girdauskas, Aleksej Rodin

Solid State Laser laboratory, Center for Physical Sciences and Technology
Savanoriu 231, LT-02300 Vilnius, Lithuania.
Email: paulius.mackonis@ftmc.lt

The progress of natural science as well as a paradigm shift in the economy became inconceivable without the implementation of superstrong electromagnetic fields. However, the commissioning of high-intensity lasers within ELI framework is more a form of budget redistribution than a solution, because the cumbersome and time-consuming laser architecture is doomed to downtime, while scientists and technologists remain on the waiting list.

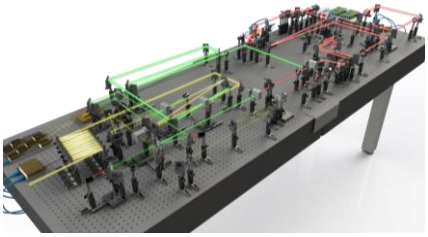

Fig. 1 Layout of high peak power laser system at FTMC.

On the contrary, a cost-effective laser system built on two 1.5 m^2 breadboards (Fig. 1) by the efforts of one graduate and 1-2 students provides a choice of output pulses: >20 mJ, 1 ps with M^2<1.1 at 1030 nm [1] or >2 mJ, <20 fs with M^2~1.2 at 790 nm [2], as well as probe supercontinuum (SC) at 600 – 2500 nm [3]. Using more pump diodes or increasing their power allows to further scale the peak power over 1 TW. Laser is based on easily reproducible modules: fiber laser front-end, two-stage double-pass Yb:YAG chirped pulse amplifier (CPA), grating compressor, SC generation, two cascades of second harmonic generation (SHG), three stages of noncollinear optical parametric chirped pulse amplifier (OPCPA), and chirped mirrors compressor. Using the same pump source for OPCPA and SC provides inherent synchronization and greatly simplifies the scheme. The energy conversion efficiency was improved due to the reuse of pump pulses depleted in SHG [1], and the maintenance of a wide OPCPA bandwidth due to their temporal shaping [2]. The solutions developed during the project were implemented at Ekspla Ltd in technological and scientific lasers. The obtained ultrashort high-energy laser pulses are ideally suited for the generation of highly efficient THz [4] and coherent X-ray radiation.

The demonstration of a multi-octave SC in the range up to 2500 nm [3] allows the use of a similar OPCPA architecture to develop a sub-TW laser in the 2 µm spectral range for the high order harmonics generation or remote sensing of gases by filamentation. However, to eliminate the need for expensive periodically poled nonlinear crystals, we are developing an alternative concept for broadband Transient Stimulated Raman Chirped Pulse Amplification (TSRCPA).

Two of the co-authors are grateful to Eksma Ltd for providing student scholarships. This research was sponsored in part by the NATO SPS Programme under grant G5734.

REFERENCES

[1] P. Mackonis, A.M. Rodin; *Opt. Express* **28** (2020) pp.1261–1268.
[2] P. Mackonis, A.M. Rodin; *Opt. Express* **28** (2020) pp.12020–12027.
[3] P. Mackonis, A. Petrulenas, V. Girdauskas, A.M. Rodin; CLEO/Europe-2019, CA-P.43 MON.
[4] J.A.Fülöp, L. Pálfalvi, S. Klingebiel, G. Almási, F. Krausz, S. Karsch, J. Hebling; *Opt. Lett* **37** (2012) pp.557–559.